Journal of Materials Chemistry C

ROYAL SOCIETY OF CHEMISTRY

PAPER

View Article Online
View Journal | View Issue

Cite this: J. Mater. Chem. C, 2025, 13, 18145

Growing ferromagnetic Fe–Ni alloy nanoparticles on nanodiamond nanotemplates: the role of sp^2-type carbon in their development and in the appearance of a martensitic-type phase†

Panagiotis G. Ziogas,[a] Athanasios B. Bourlinos,[a] Polyxeni Chatzopoulou,[b] George P. Dimitrakopulos,[b] Anastasios Markou[a] and Alexios P. Douvalis*[a]

This work presents a novel hybrid nanostructured magnetic material consisting of ferromagnetic (FM) fcc Fe–Ni nanoparticles (NPs) grown on nanodiamond (ND) nanotemplates. The development of this hybrid magnetic nanomaterial is realized through the combination of wet chemistry and thermal annealing under vacuum. The characterization and study of the prepared samples, which were performed using a range of specialized experimental techniques, reveal that thermal annealing of the as-made hybrid precursor under a range of different conditions leads to the growth of fcc Fe–Ni alloy NPs at the surfaces of the ND nanotemplates. These alloy NPs have an average size of 10 nm, exhibit uniform distribution on the ND nanotemplates and have a predominant nickel content of approximately 64 at%. They demonstrate FM behavior throughout a temperature range from 2 K to 400 K, with maximum magnetization values ranging between 8.6 and 11.9 emu g^{-1} and coercivities ranging between 10 and 610 Oe. Moreover, ^{57}Fe Mössbauer spectroscopy reveals that apart from the predominant fcc FM Fe–Ni phase, iron atoms also participate in the formation of a secondary martensitic-type Fe–Ni phase, the development of which is attributed to the partial diffusion of carbon atoms at interstitial sites within the Fe–Ni lattices during the alloy NP formation at elevated temperatures, as a consequence of the unique morphological properties of the ND growth matrices, which facilitate surface formation and reconstruction of sp^2 nanostructures. Concurrently to their diffusion within the Fe–Ni NP lattice, the carbon atoms are also found to reconstruct layered graphitic-type nanostructures enveloping the metallic alloy NPs, but only where ND NPs are adjacent. These non-typical nanohybrid materials hold significant potential for use in applications related, but not limited to biomedicine, biopharmaceutics, catalysis, and other various contemporary technological fields.

Received 12th March 2025,
Accepted 21st July 2025

DOI: 10.1039/d5tc01095k

rsc.li/materials-c

1. Introduction

Today, technology offers opportunities to overcome great challenges, but at the same time entails the involvement of more complicated processes. This growing complexity makes imperative the need for employment of sophisticated materials to carry out these demanding processes efficiently. On the other hand, it is also important from environmental and economical aspects that these materials must be characterized by long-lasting high performance and should be derived from eco-friendly and low-cost synthetic procedures.

Hybrid materials that combine different types of materials blended in a single entity exhibit such advantages and the diversity of their properties enables them to be used in a wide variety of applications, from automotive and construction to electronics, pharmaceutical and biomedical fields.[1] Moreover, the properties of hybrid materials are considered more effective when synthesized at the nanoscale.

Among a wide variety of nanohybrid materials (or simply nanohybrids – NHDs), metal compound hybrids are of great interest.[2] These NHDs involve the development of nanosized metallic compounds on the surface of an appropriate growth platform material. Such promising candidates with well-established physical properties suitable to serve as growth matrices are the nanodiamonds (NDs).

On the nanoscale, diamond nanocrystals stand out among many materials, including other nanocarbon allotropes. Typically, NDs manifest extreme mechanical robustness and

[a] Physics Department, University of Ioannina, 45110 Ioannina, Greece. E-mail: adouval@uoi.gr
[b] Physics Department, Aristotle University of Thessaloniki, 54124 Thessaloniki, Greece

† Electronic supplementary information (ESI) available. See DOI: https://doi.org/10.1039/d5tc01095k

excellent thermal conductivity and are already used in cutting, drilling, and semiconductor manufacturing applications. Moreover, NDs exhibit great biocompatibility, ultra-low toxicity, and superior chemical stability compared to other nanocarbon allotropes.[3] Hence, NDs are ideal candidates for fields like biomedicine and biopharmaceutics (*e.g.*, in bioimaging,[4] biosensing techniques,[5] drug delivery,[6] hyperthermia,[7] and as contrast magnetic resonance imaging (MRI) agents[8]).

The implementation of NDs in various technological fields and applications is owing to their very stable crystal structure. The structural stability of NDs arises from their unique sp^3 bond hybridization, which, in combination with their versatile morphology, provides them with many interesting features. Regarding their morphology, commercially available pristine detonation ND nanoparticles (NPs) are spherical, crystalline, and monodisperse, with an average NP size of about 4 to 5 nm. Furthermore, these ND NPs are sintered to larger cluster structures appearing as close-up agglutinates.[9–11] These agglutinates can display fractal morphologies of a few NPs in thickness and from a few tens to several hundred nanometres in length. Therefore, NDs can be arranged in robust substrates of clustered diamond NPs, providing favourable conditions for exploitation as prospective growth platforms for numerous applications where particle aggregation and surface phenomena are of great importance.[10]

Moreover, diamond NPs present an ultrahigh surface-to-volume ratio. This morphological feature enables the interaction of a significant part of diamond carbon atoms at the surface and subsurface regions of the NDs. Nevertheless, these nano-scaled regions are most likely to be influenced by imperfections and defects, derived from the NDs' detonation reaction origins, which prompt deviations from the nominal periodicity in the solid. As a result, a significant portion of unsaturated carbon atoms can be observed in the superficial and subsuperficial ND sites, which, consequently, undergo significant surface relaxation phenomena either (i) through their stabilization with hydrogen and oxygen functional groups under ambient conditions, rendering these surface terminations a significant parameter for regulating the chemical stability of NDs[3,9] or (ii) through their structural reconstruction *via* thermal treatments at elevated temperatures, into full and/or partial sp^2 hybridized domains in order to reduce the ND surface energy.[3,9,11] The thermal treatment of carbon nanostructures enables the fabrication of sp^3 bond hybridized NDs into either consistent or partially sp^3/sp^2 core/shell hybrids or concentric layers of sp^2 graphitic carbon onions, depending on the annealing conditions. As a result, these engineered NDs are anticipated to be valuable for investigating interfacial–surfactant interactions. In addition, diamond nanocrystals can be surface-modified with appropriate functional groups to enable the coupling of various organic and/or inorganic compounds to enrich their properties and, as such, the application prospects of a corresponding proposed hybrid system. The coupling bonds of various compounds with the diamond nanocrystals determine to a large extent the physicochemical properties of the resulting NHD materials and provide new characteristics not shown by the diamond nanostructures alone.[9,11–13]

On the other hand, within the scope of discovering new materials for society' s ever-growing global needs, well-known compounds that can be modified to develop extraordinary properties present a significant prospect. In this concept, the iron–nickel (Fe–Ni) alloy system stands out as a prime example of a traditional engineering and magnetic material that presents highly renewed interest due to the potential to enhance its properties by introducing interventions in its crystal structure. These interventions combined with a relative frame of growth could develop novel metal compound hybrids. Historically, Charles Edouard Guillaume was the first scientist to introduce Fe–Ni alloys, and he received the Nobel Prize in Physics for his discovery of the Invar alloy.[14,15] This iron–nickel alloy, containing 36 at% Ni, exhibits an extremely low thermal expansion coefficient over a wide range of temperatures around ambient temperature. In addition to the interesting and widely exploited thermal properties of the Invar alloy, the Fe–Ni system has garnered immense interest for its magnetic properties over the last decade. The equilibrium Fe–Ni phase diagram generally exhibits two major single-phases, α and γ, and a two-phase $\alpha + \gamma$ region. The α phase refers to a body centered cubic (bcc) ordered crystal lattice, called kamacite, which does not accept more than 5 to 7 at% Ni concentration. The γ phase refers to a face centered cubic (fcc) disordered crystal lattice, called taenite, which occurs in a wide range of Ni concentrations and extends at high temperatures above 400 °C. Kamacite exhibits soft ferromagnetic (FM) characteristics at and above room temperature (RT) up to its Curie temperature (T_C) of $\sim$900 °C[16,17] since its formation occurs above the T_C of pure iron, while taenite, due to its disordered crystal nature and higher Ni content, presents paramagnetic (PM) characteristics at high temperatures and lower T_C values compared to kamacite. However, the high-temperature PM γ-phase of taenite decomposes into two disordered phases as the temperature decreases. One is a PM fcc disordered γ_1-phase with low Ni concentration up to 28 at% Ni, named anti-taenite.[18] The other is a FM fcc disordered γ_2-phase with high Ni concentration from 45 up to 70 at% Ni, called high-Ni taenite, which is encountered across the phase diagram above 330 °C.[19] Studies on the Fe–Ni phase diagram below 400 °C demonstrate an extensive asymmetrical miscibility gap associated with a magnetically induced spinodal decomposition for alloys containing 28–45 at% Ni.[20–22] Moreover, between the metastable phase boundaries of low Ni compositions containing 7 to 27 at% Ni, martensitic transformations are also observed.[23]

For a considerable time, the phase transformations of the Fe–Ni system at low temperatures were shrouded in ambiguity, rendering this phase diagram as complex and not well understood. Another significant challenge involved in the studies of these alloys is the low diffusion rates of the metal atoms in the Fe–Ni system at low temperatures such as those below 400 °C. R. B. Scorzelli *et al.* and many other groups have reported that as cooling occurs, the diffusion coefficient of Ni in taenite decreases from 1.5×10^{-16} cm^2 s^{-1} at 600 °C to 1×10^{-21} cm^2 s^{-1} at

500 °C. Remarkably, at 300 °C, it would take more than 10^4 years for one Ni atomic jump to occur.[20,24–26] For this reason, many scientists were called upon to shed light on and to resolve the low-temperature phase transformations of the Fe–Ni system. In 1962, J. Paulevé *et al.* demonstrated for the first time, by conducting neutron irradiation experiments in the presence of a magnetic field on equiatomic FeNi alloys, a new order–disorder transition to an ordered crystal phase of the AuCu-type at 320 °C.[27] This chemically ordered equiatomic FeNi γ''-phase, called tetrataenite, exhibits a tetragonal structure with a tetragonal-base lattice constant of a = 3.582 Å and c/a ratio very close to 1. Magnetic studies have revealed that this tetragonal $L1_0$ FeNi phase is a promising hard magnet, offering a large uniaxial magnetic anisotropy constant, $K_u \sim 7 \times 10^6$ J m^{-3}, and a high T_C of ~550 °C.[28] Such a significant discovery led to the study of the ordered FeNi alloy with the $L1_0$ structure by several groups,[23,27] highlighting neutron irradiation as a non-conventional method to enhance atomic diffusion in sluggish (referring to the low diffusion rates) systems at low temperatures.

It is generally accepted that both diffusion effects and fast particle irradiation are closely connected. In particular, as an excess number of defects can be produced by irradiation, defects tend to maintain a steady concentration during irradiation at elevated temperatures. This steady-state concentration of excess defects is directly related to higher diffusion, and therefore, regulating the particle irradiation can subsequently improve the diffusion rate in materials such as the Fe–Ni alloys.[29]

Nonetheless, despite the extensive studies of the ordered $L1_0$ FeNi phase, there are still unanswered questions concerning the characteristics of the phases cohabiting in the renewed Fe–Ni phase diagram. However, answers emerged surprisingly from a rather, at that time, unexpected source, as they came from studying the properties of the residual meteorite cores falling from the sky, providing tons of insightful information regarding this challenging system. Iron meteorites are interesting natural systems composed of Fe–Ni alloys that have cooled at a rate of about 1–10 °C per 10^6 years.[23] This unique cooling rate provides an opportunity to thoroughly study Fe–Ni alloys in thermodynamic equilibrium, compared to alloys prepared in the laboratory. Therefore, iron meteorites have played a significant role in the study of the Fe–Ni phase diagram. Most meteorites, similarly to the synthetic samples, are composed mainly of two phases one corresponding to kamacite and one corresponding to taenite. These two phases possess definite crystallographic orientations relative to each other, forming a pattern called Widmannstätten. This pattern can be arranged with unchanged orientations throughout the entire meteorite, showing that originally the meteorite, at a higher temperature, was an fcc crystal. However, the very slow cooling process allowed plates of kamacite to precipitate along the appropriate planes of the fcc crystal. Subsequent growth of the kamacite regions led the meteorite to be composed of alternating and/or intersecting regions of kamacite and taenite of the original fcc crystal.[21]

Many investigations have pointed out a complex morphology in the microstructure of meteoritic taenite, generally occurring as thin plates called lamellae, composed of an ordered FM equiatomic FeNi phase (tetrataenite) with the $L1_0$ γ''-phase superstructure and a disordered PM fcc Ni-poor γ_1-phase Fe–Ni alloy (anti-taenite). Structural studies show that both FM γ'' and PM γ_1 phases have the same lattice constants, about 3.582 Å, forming together a pseudo-monocrystal, whose axes are those of the original high-temperature fcc crystal, as mentioned above. Also, many studies on meteoritic samples have shown that kamacite consists of up to 8 at% Ni concentration and is well defined in the Fe–Ni phase diagram. These studies also indicate instabilities regarding the taenite lamellae, which present steep nickel concentration gradients near the interface between kamacite and taenite and moving inwards from this interface into taenite, a wide layer containing 40–50 at% Ni is encountered. This surface layer of the lamellae is composed mainly of the ordered $L1_0$ FeNi phase, while deeper in the lamellae follows a ''dark-etching'' layer containing about 28–45 at% Ni. This layer consists of fine domains of the ordered FeNi phase and a PM disordered γ_1-alloy with less than 28 at% Ni in between, rather than an fcc Fe–Ni alloy with continuously varying composition.[22]

J. F. Albertsen *et al.* indicated that the observation of a monomineralic layer of tetrataenite and of anti-taenite/tetrataenite intergrowths suggests that the stability range of tetrataenite at the equilibration temperature (320 °C) is between 46 and 53 at% Ni.[22] Furthermore, bulk fcc Fe–Ni alloys with less than about 28 at% Ni transform by a diffusion-less process to another important metastable phase called martensite (α_2-phase). Nonetheless, well-distributed small crystallites of the disordered γ_1-phase Fe–Ni alloy (with less than 28 at% Ni) are known to be unstable towards martensitic transformation at and below RT. This instability is likely due to the intimate intergrowth of the γ_1-phase, with the ordered $L1_0$ phase on the same Bravais lattice, thereby stabilizing both of them in the fcc structure.[21] Finally, an inner layer found only in thick lamellae is entirely transformed into the α_2 martensite phase. The occurrence of martensite in the middle of the lamella is consistent with the decreasing Ni-concentration towards the centre of the lamellae, as fcc Fe–Ni alloys with low nickel content are unstable towards martensitic transformations.[30] Moreover, in the centre of some thick lamellae, the α_2 phase decomposes into a combination of α and γ phases called plessite. In contrast, thin lamellae contain no martensitic α_2 phase. Apart from the equiatomic ordered FeNi crystal structure, another ordered structure exists in the Fe–Ni alloy system. This compound, with a high Ni concentration of about 75 at% Ni, possesses an ordered soft FM γ'-fcc crystal $AuCu_3$-type $L1_2$ structure (space group *Pm*3*m*) called awaruite.[23,31] Comprehensive studies undertaken on many iron-meteoritic samples have led to a thorough characterization of the Fe–Ni phases observed in the low-temperature phase diagram range and have helped to reveal the elusive and complicated interconnections between them. Thus, the discovery and interpretation of the ordered $L1_0$ FeNi tetrataenite, whether by artificial or natural means, have

intensified the interest in exploiting its unique magnetic properties.

Compared to other metallic minerals, tetragonal $L1_0$ tetrataenite features very high coercivity values, between 1500 and 3000 Oe at RT, and a uniaxial magnetic anisotropy constant K_u of about 1.5×10^6 J m^{-3} at RT,[32–35] associated with strong perpendicular magnetocrystalline anisotropy. This significant anisotropy energy value is attributed to tetrataenite's chemically ordered tetragonal crystal structure, positioning γ''-FeNi as a promising permanent magnet candidate with a theoretical maximum energy product of 335 kJ m^{-3}, roughly 66% of that of NdFeB-based supermagnets.[36] Moreover, many studies based on a wide variety of iron-meteoritic samples report coercivity values in the range of 1100 to 3000 Oe and saturation magnetization (M_S) values of about 135–150 emu g^{-1} for tetrataenite at RT.[33] Additionally, tetrataenite, although presenting high T_C (550 °C), due to its chemical stabilization at low temperatures, exhibits also a low chemical order–disorder temperature of T_{O-D} = 320 °C.[27] These favourable magnetic properties render tetrataenite as a superior magnetic material comprised of inexpensive, easy-to-process, readily available and free from rare-earth elements. These appealing features position tetrataenite as a feasible and promising permanent magnet candidate with the potential to supplement and/or replace rare-earth permanent magnets for energy transformation and generation. Additionally, this intriguing magnetic material can provide effective magnetic properties, making it suitable for exploitation in electronics, such as in microwave devices and electromagnetic wave-absorbing materials,[37] or in medical science applications such as ferrofluids for use in magnetic hyperthermia,[7] MRI[8] and drug delivery.[38]

Unfortunately, engineering the fabrication and stabilization of the tetragonality and long-range chemical ordering in the chemically disordered fcc parent Fe–Ni phase to form tetrataenite has proven to be very challenging. Since atomic diffusion is extremely slow at the order–disorder temperature point, an inconceivably long amount of time would be required to synthesize $L1_0$-FeNi. Therefore, $L1_0$-FeNi with a significantly high long-range order parameter, S, cannot be derived through the conventional equilibrium process that promotes the formation of $L1_0$ through a mutual diffusion of Fe and Ni, utilizing the stability of $L1_0$-FeNi as the driving force for ordering.[32,33,36]

As mentioned earlier, to enhance diffusivity towards the γ''-FeNi phase formation, it is necessary to increase the material's defect concentration, which has primarily been managed through neutron irradiation. Considering this, many research groups have tried to implement similar tactics using different synthetic routes. In some cases, the importance of induced tetragonal distortion towards the stabilization of the peculiar tetragonal $L1_0$ FeNi alloy phase is highlighted. This mechanism can be achieved in two ways: (i) by applying uniaxial stress to the parent Fe–Ni lattice through epitaxial effects or (ii) by introducing a third element, such as boron (B), nitrogen (N), or carbon (C) atoms, interstitially into the parent fcc taenite Fe–Ni structure.[39–41]

Regarding the latter method, Goto *et al.* proposed an ordered-alloy formation process involving a stable ordered intermediate material. In this method, the ordered configuration of FeNi is triggered by nitriding the metal structures, combined with the following topotactic de-nitration to extract nitrogen atoms from the FeNi nitrides without damaging the crystal structure. $L1_0$-FeNi fabricated by this method showed a high coercive field of 1800 Oe, along with a high K_u value of about 1×10^6 J m^{-3}, which is directly correlated with the high degree of order ($S \sim 0.7$) in the material. While this K_u value is less than that of Nd–Fe–B (4.9×10^6 J m^{-3}), it is still an extremely high value considering that the material is free of rare-earth elements. The proposed method, called nitrogen insertion and topotactic extraction, is demonstrated as an effective alternative for fabricating $L1_0$-FeNi, differentiating from the conventional thermally activated process in that the ordered alloys can be derived directly by de-nitriding.[33] Since that effort, many other studies have followed, based on this synthetic process. Recently, F. Takata *et al.* developed for the first time single-phase tetragonal Fe_2Ni_2N films by molecular beam epitaxy, which, after a subsequent extraction of N atoms, led to the formation of FeNiN films with an $L1_0$ tetragonal crystal structure. This approach, proceeding from the fabrication of high uniaxial magnetic anisotropy $L1_0$ FeNiN epitaxial films followed by a 100% extraction of N atoms, could advance the development of well-ordered tetragonal FeNi films.[42]

Similarly, M. Gong and S. Ren, reported a rational epitaxial core–shell compound based on the heteroepitaxial growth of AuCu/FeNi core–shell NPs, which stabilizes the tetragonal FeNi shell phase revealing enhanced coercivity and anisotropy. The key element for achieving this unique magnetic performance ($H_C \sim 1010$ Oe and $M_S \sim 122$ emu g^{-1}) is the realization of a tetragonal distortion induced by the $L1_0$ phase transformation of the AuCu core. This transformation transfers the necessary strain energy on the epitaxial interface to trigger and stabilize the tetragonal FeNi structure.[32]

Significant theoretical research has also provided a robust platform for studying alloying effects with the ultimate goal of stabilizing the $L1_0$ FeNi compound. For instance, L. Y. Tian and co-workers, focusing on the phase transformation of the tetragonal FeNi phase based on first-principles theory, found a strong dependence of the T_{O-D} on the configurational and vibrational degrees of freedom. Their calculations yield a final T_{O-D} = 286 °C compared to the experimental value of 320 °C. Their results open up the possibility of developing an effective and accurate method for modelling tetragonal ordered forms of FeNi alloys.[28] In this context, many other theoretical studies have emphasized the need to stabilize $L1_0$-FeNi compounds by introducing tetragonal distortions. To promote the formation of the $L1_0$-FeNi crystal structure, researchers have proposed doping with other elements, like C, B, and hydrogen (H), in addition to N.[34,43–45] In particular, P. Rani *et al.* in their study investigated the regulation of the magnetocrystalline anisotropy of $L1_0$-FeNi by the diffusion of interstitial carbon-doped atoms using a full-potential approach within the generalized gradient approximation. Their calculated results showed a

significant K_u value of 1.9 × 10^6 J m^{-3}, due to a feasible tetragonal distortion induced by interstitial carbon-doping followed by a slight decrease in M_S.

Considering the significance of all these Fe–Ni alloy magnetic characteristics, in our current study we conducted a thorough investigation into the synthesis, characterization, and analysis of the interconnected structural, morphological, and magnetic properties of a new line of hybrid nanostructured magnetic materials composed of Fe–Ni nanoalloys grown on ND nanotemplates (Fe–Ni/NDs). This research builds on our group's expertise in the development of such hybrid nanostructured magnetic materials.[46–49] The realization of these nanohybrid structures was achieved using a two-step synthesis procedure: a wet chemical impregnation method that was aimed to produce an as made-nanohybrid (AM-NHD) precursor, followed by subsequent thermal treatments under controlled conditions, that involved heating of this precursor in evacuated quartz ampoules at 700 °C for 30 min (NHD-700C,30m) and 4 h (NHD-700C,4h), to realize the final Fe–Ni/ND samples (details are given in Section 4.1 Materials synthesis).

We characterized and studied these samples using X-ray diffraction (XRD), transmission electron microscopy (TEM) and high-resolution TEM (HRTEM), scanning TEM (STEM) with high-angle angular dark-field (HAADF) imaging and energy dispersive X-ray spectroscopy analysis (EDS), vibrating sample magnetometry, and ^{57}Fe Mössbauer spectroscopy techniques. The results indicate that the stability and nature of the nanostructured phases developed on the surface of the ND nanotemplates are determined by the annealing conditions (temperature and annealing duration). In all samples, the formation of a dominant component corresponding to the nanostructured FM $FeNi_3$ alloy phase is evident, along with a significant and systematic contribution of a tetragonally distorted martensitic-type Fe–Ni:C phase. It is suggested that the latter phase emerges from the diffusion of carbon atoms into the crystal structure of the Fe–Ni phase, promoted by the interfacial interactions between the growing Fe–Ni magnetic NPs and the sp^2 type surfaces of the ND nanotemplates.

This nanohybrid system, reported here for the first time, shows promising structural and magnetic features suitable to be exploited in various modern and innovative technological fields, and in particular, due to the high biocompatibility of its components, it can be suggested to be used in magnetic hyperthermia and MRI contrast agent related applications. Furthermore, studying the martensitic-type Fe–Ni phase in these samples could offer insights into creating similar tetragonally distorted structures. This could advance the development of new hard FM materials that do not rely on rare-earth elements.

2. Results and discussion

2.1 XRD

Fig. 1 depicts the XRD diagrams of a typical first-step synthesis AM-NHD precursor, along with the following annealed samples at 700 °C for different heating durations, 30 min and 4 h.

For the AM-NHD sample (Fig. 1 bottom) the presence of the main diffraction peaks of the cubic ND structure at 43.9 (111), 75.3 (220) and 91.5 (311) degrees 2θ (lattice constant a = 3.567 Å, ICDD PDF 00-006-0675) and that of the iron-nickel spinel oxide $Ni_xFe_{3-x}O_4$ (INO) structure at 30.3 (220), 35.7 (311), and 63.1 (440) degrees 2θ (lattice constant a = 8.3337 Å, ICDD PDF 00-054-0964),[50] respectively, is observed. An estimation of the average NPs' crystalline domain size $\langle D \rangle$ for each one of these two phases, based on the most resolvable widths of their main diffraction peaks, was made using the Scherrer formula,[51] providing an average size of $\langle D_{NDs} \rangle$ = 4 nm for the NDs and $\langle D_{INO} \rangle$ = 2 nm for the spinel oxide NPs. These results evince the development of very small spinel oxide NP seeds on the ND nanotemplate matrices for the AM-NHD precursor.

Furthermore, treating thermally the AM-NHD precursor at the chosen temperature and time durations promotes the formation of a new prominent nanocrystalline phase (Fig. 1 middle and top), which is accompanied by the retained presence of the NDs, while that of the spinel oxide phase is seemingly diminished. More specifically, the presence of the characteristic ND diffraction peaks is followed by considerable contributions from the broad diffraction peaks of a cubic fcc Fe–Ni crystal structure, which are evident at 43.8 (111), 51.1 (200), 75.1 (220), 91.2 (311) and 96.6 (222) degrees 2θ for the measured XRD diagrams of the annealed samples. Due to the relatively large width of this phase's diffraction peaks, it is difficult to make an accurate determination of the atomic Fe–Ni ratio based on their angular positions, since three different ICDD PDFs, representing iron-rich ($Fe_{0.7}Ni_{0.3}$ ICDD PDF 01-071-8325 lattice constant a = 3.575 Å), equiatomic ($Fe_{0.5}Ni_{0.5}$ ICDD PDF 01-071-8322 lattice constant a = 3.575 Å), and iron-poor ($Fe_{0.3}Ni_{0.7}$ ICDD PDF 01-074-5840 lattice constant a = 3.564 Å) Fe–Ni stoichiometries, can match qualitatively at the same level these diffraction peaks. The nature, morphology, and stoichiometry of this phase in the samples are elucidated through TEM analysis (*vide infra*). Nevertheless, the average crystalline domain size $\langle D \rangle$ can be estimated from the most clearly resolved width of the (200) diffraction peak at 51.1 degrees 2θ for this phase using the Scherrer formula, as illustrated in each diagram of Fig. 1. The average Fe–Ni metallic NP size drops to a narrow range between 7 and 9 nm for the two annealed samples, with the higher value corresponding to the sample with the longer annealing duration. Based solely on these XRD findings, it is suggested that the formation of the Fe–Ni alloy phase from the reduction of the spinel oxide NP seeds can be sufficiently realized at 700 °C, without the presence of any residual spinel oxide phase, whose existence however could not be excluded at all, as it could be present in the form of very small residual NPs that, due to their reduced size, are not contributing sufficient signal to overcome the diffractogram's noise. At the same time, the different annealing durations of 30 min and 4 h seem not to affect significantly the average particle size, nor the presence of any residual non-reduced spinel oxide phase in the samples, suggesting that the Fe–Ni alloy phase can be formed within a short period of time during the annealing process.

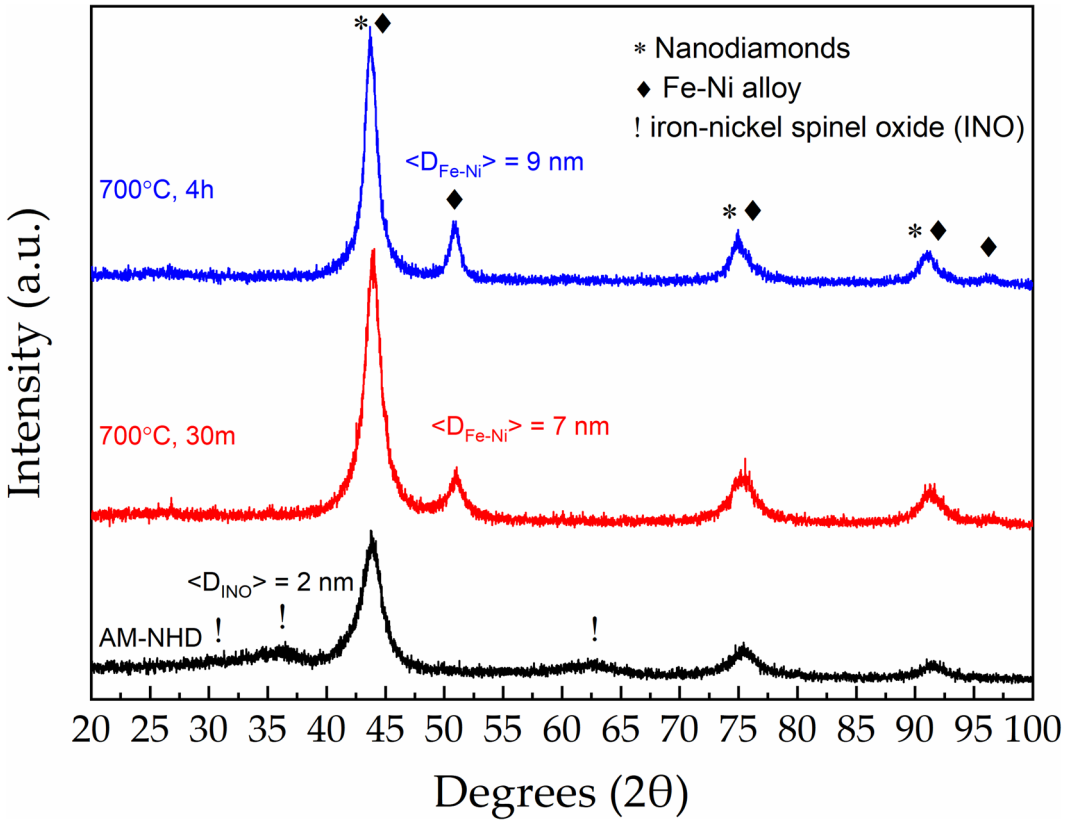

Fig. 1 XRD diagrams of the as-made nanohybrid precursor (bottom) and the corresponding annealed samples for 30 min (middle) and 4 h (top) at 700 °C. The crystalline phases in the samples are depicted by the relative different symbols denoting the angular positions of their main diffraction peaks. The average crystalline domain size ⟨*D*⟩ of the iron–nickel spinel oxide phases for the as-made nanohybrid precursor sample and that of the Fe–Ni alloy phase for all other samples are denoted in each diagram.

2.2 Analytical electron microscopy

(S)TEM was utilized to determine the size distribution and stoichiometry of the metallic NPs, while HRTEM was employed to further reveal their crystal structure and the interfacial properties of the metallic NP/ND heterostructures. Representative TEM images of the NHD-700C,4h sample are given in Fig. 2. A homogeneous dispersion of ND coarse agglutinate clusters of arbitrary shapes and sizes ranging from 35 to 120 nm was observed.

These ND clusters host well dispersed roughly rounded-shaped metallic NPs developed on their surface, which appear with darker contrast compared to the ND NPs, due to their higher mass density.

To resolve better the distribution of metallic NPs on the hybrid structures, HAADF imaging in STEM mode was used, as its contrast is directly related to the atomic number. Fig. 3a–c display HAADF-STEM images, illustrating the distribution of metallic NPs on various hybrid clusters. In Fig. 3d, the metallic NP size dispersion is presented, revealing an asymmetric distribution, with a wider spread towards larger sizes and an average size of 10 nm. EDS elemental maps from an NHD cluster are shown in Fig. 3f and g. It is apparent that Fe and Ni atoms occupy identical positions, confirming the formation of the Fe–Ni alloy. Further point EDS spectra from individual metallic NPs, as shown in ESI,† Fig. S1, and Fe compositions as listed in the ESI,† Table S1, suggest that the Fe–Ni alloy phase is predominantly Ni-rich, with an average atomic ratio of Fe : Ni being approximately 36 : 64 ($Fe_{36}Ni_{64}$).

Moving forward, Fig. 4 displays HRTEM images of different metallic Fe–Ni NPs developed on the surfaces of the ND nanotemplates, where the characteristic *d*-spacings attributed to the close-packed {111} planes and the {002} planes of the fcc $Fe_{36}Ni_{64}$ alloy are well resolved. Moreover, as indicated by a blue pseudo colour, few-layered graphitic-type continuous structures are found to develop at the interface between the metallic Fe–Ni NPs and the carbon support assembly. These graphitic-type structures are found to partially wrap the metallic Fe–Ni NPs, appearing only in regions where direct contact with the carbon nanostructured supporting template exists. This is shown in more detail by the white borderline in Fig. 4a, which defines the edge limit of the carbon support.

At the same time, the presence of the graphitic-type layered structures has been consistently observed in numerous other Fe–Ni NPs studied in this sample (see Fig. S2, ESI†).

Based on these TEM observations, it is evident that the development of the graphitic-type layered structures is closely interconnected to the unique morphological features of the NDs in these nanotemplates and the way they are influenced by

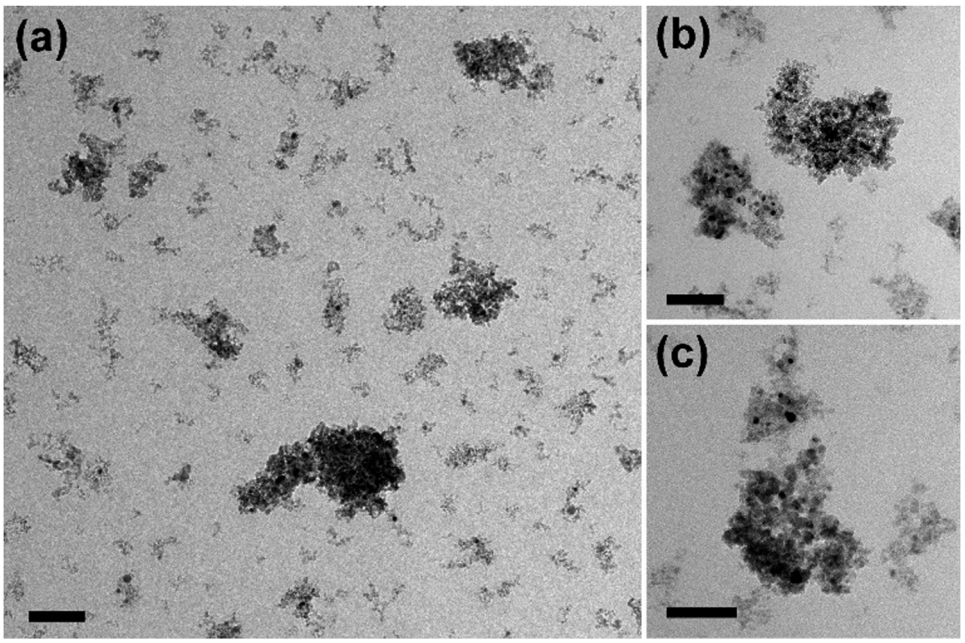

Fig. 2 Bright-field TEM images of the NHD-700C,4h sample (a)–(c) at different magnifications. The scale bars correspond to 100 nm.

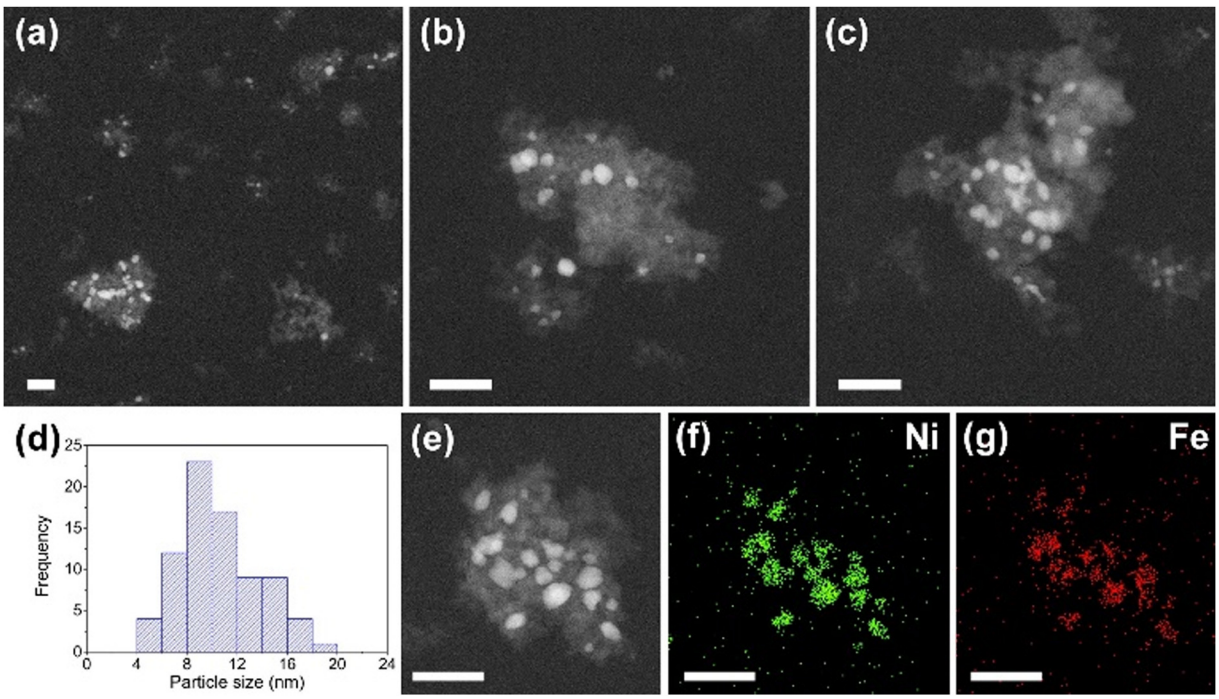

Fig. 3 HAADF STEM images of different NHD clusters of the NHD-700C,4h sample (a)–(c). Distribution of the Fe–Ni metallic NP sizes (d). HAADF STEM image of a particular hybrid Fe–Ni NP/ND cluster (e) and the corresponding elemental distribution of Ni (f) and Fe (g). All scale bars correspond to 50 nm.

temperature, as well as the way they interact with the growing Fe–Ni NPs. In addition, their regular formation on the surfaces of the grown Fe–Ni NPs, but only where there is a direct contact with ND NPs, indicates a strong affinity of these sp^2 graphitic nanostructures towards the metallic compounds, which emphasizes the essential role of carbon for their development. Based on this argument, the verified presence by TEM observations of these carbon atom graphitic-type layers at the interface between the Fe–Ni metallic and ND NPs and their consequent physicochemical interactions can also suggest the further possible diffusion of C atoms within the Fe–Ni alloy structure.

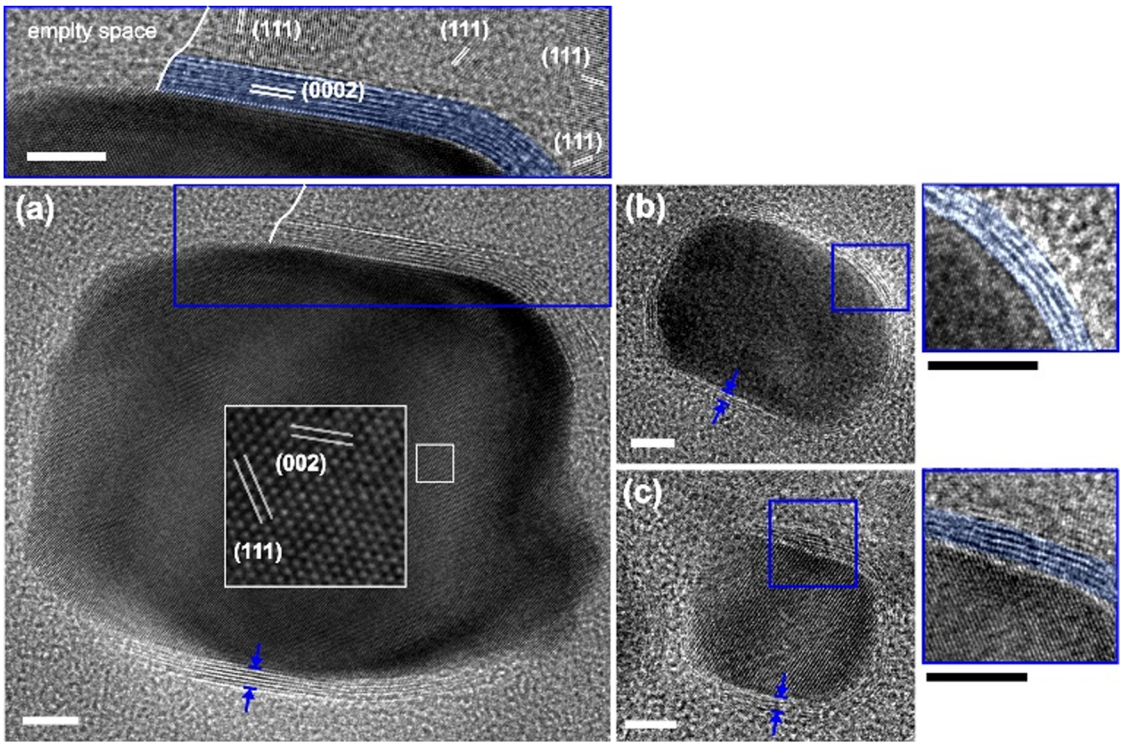

Fig. 4 HRTEM investigation of the NHD-700C,4h sample. The Fe–Ni NP in (a) sits at the edge of a hybrid cluster and is viewed along the [1Mx0̄31;0] zone axis. The (111) and (002) planes of the fcc FeNi alloy are indicated. In the magnified inset (a) top, the characteristic (0002) close-packed planes indicate the formation of few-layered graphite (blue pseudo colour) at the interface between the Fe–Ni NP and the carbon nanotemplate. Close-packed {111} planes, coming from small ND crystallites, are also indicated. The white line delineates the border of the ND nanotemplate. HRTEM images of other Fe–Ni metallic NPs, showing the formation of few-layered graphite of similar thickness (b) and (c). All scale bars correspond to 5 nm.

2.3 ^{57}Fe Mössbauer spectroscopy

The iron-containing phases developed in the NHD samples are further investigated by the atomic-level-probing characterization and study technique of ^{57}Fe Mössbauer spectroscopy, giving insights for their structural, morphological and magnetic properties. The ^{57}Fe Mössbauer spectra (MS) of the AM-NHD precursor and the NHD-700C,30m and NHD-700C,4h annealed samples recorded at RT (296 K) are presented in Fig. 5–7, while additional MS of these samples collected at 77 K are given in the ESI† (Fig. S3). In Fig. 5, the spectrum of the AM-NHD precursor is characterized by only one quadrupole split contribution with relative broad resonant lines. Attempting to fit this spectrum with only one quadrupole split component didn't give sufficient fitting results, forcing us to include two different quadrupole split components in the fitting model, which improved the quality of the fit substantially. The resulting Mössbauer parameters (MPs) values from the best fit of this spectrum are listed in Table 1. These values indicate the presence of Fe^{3+} high-spin (S = 5/2) states for both components (SPM Fe^{3+} (1) and SPM Fe^{3+} (2) coloured dark cyan and purple in Fig. 5 respectively) that are characteristic of Fe^{3+} ions found in spinel oxide nanostructures, for which their particle size is so small that it renders them superparamagnetic (SPM) characteristics at RT.[52–56] This finding verifies the respective result regarding the average particle size of 2 nm deduced for this phase from the XRD measurements of this sample. At this temperature, the sizes of all spinel oxide NP seeds developed on the surfaces of the ND nanotemplates during the first step of the synthesis of the AM-NHD precursor sample drop below the SPM size limit, where the SPM relaxation is so fast that the characteristic relaxation time τ is shorter than the characteristic ^{57}Fe Mössbauer spectroscopy measuring time τ_{MS}, which is of the order of $\sim 10^{-8}$ s, and consequently, their hyperfine magnetic field (B_{hf}) values average to zero (collapse completely).[57,58] By lowering the temperature to 77 K, for a significant part of the spinel oxide NP seed assembly, τ is increased to comparably and slightly higher values relative to τ_{MS}, conferring to these NPs magnetic splitting and collapsing B_{hf} characteristics in their relative contribution to the corresponding Mössbauer spectrum (Fig. S3a, ESI†). This part is represented by the MCOL Fe^{3+} component coloured red in Fig. S3a (ESI†). These are most probably the spinel oxide NPs with the larger sizes in the particle size distribution and/or the NPs, which are in closest proximity to each other.[59,60] For the remaining part, which corresponds to the smaller size and/or more isolated spinel oxide NP seeds, the SPM characteristics are retained at the 77 K spectrum. This part is represented by the two quadrupole split SPM Fe^{3+} (1) and SPM Fe^{3+} (2) components at this temperature similar to what was found at RT.

The MS of the annealed samples are shown in Fig. 6 and 7. Regardless of the annealing duration, both spectra display similar characteristics, which can be described qualitatively by: (i) a set of rather broad but distinct magnetically split

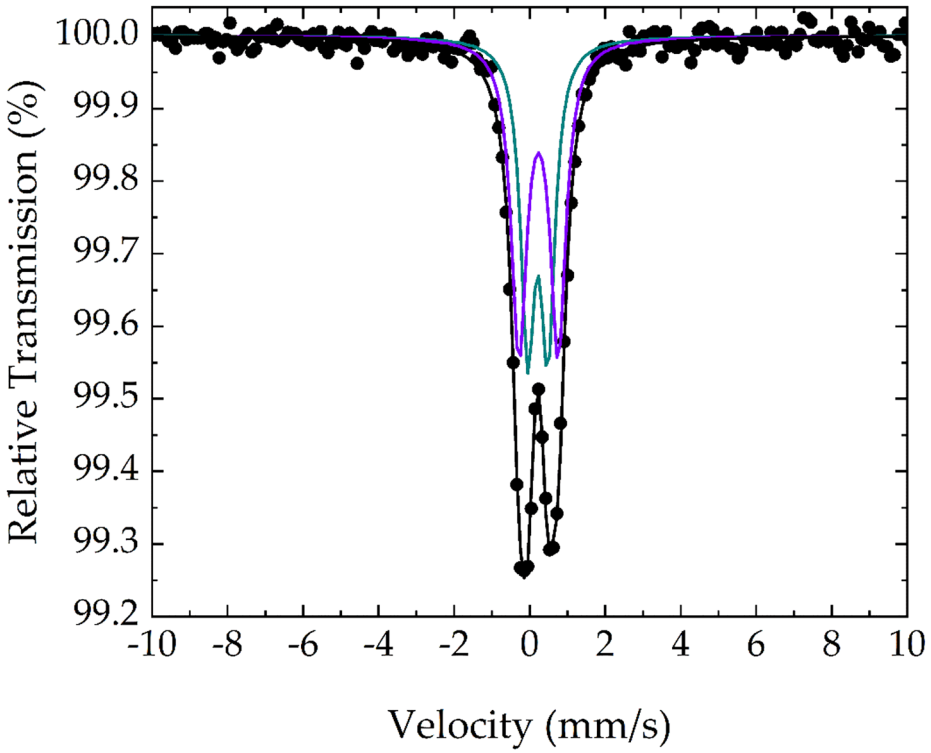

Fig. 5 ^{57}Fe Mössbauer fitted spectrum of the AM-NHD precursor collected at room temperature. Points represent the experimental data and the coloured lines the components used to fit the spectrum.

contributions accompanied by (ii) a set of minor magnetically split contributions detected mainly as satellites around the outer resonant peaks of the distinct magnetically split contributions and (iii) a set of quadrupole split contributions observed at the center of the MS. The intensity of the distinct and satellite magnetically split contributions (i) and (ii) is relatively stable in each of these two MS, but that of the quadrupole split contributions (iii) is more pronounced for the sample annealed for the shorter annealing duration (30 minutes), compared to that found for the sample annealed for the longer annealing duration (4 hours).

Analysing adequately such complex MS is a challenging endeavour, since different sets of fitting models can be used. To reach a solid choice on the fitting model, we considered the facts already gained from the other experimental characterization techniques in this study, namely XRD and TEM. The main evidence obtained from these two experimental methods is: (a) there is a dominant presence of an fcc Fe–Ni nanostructured alloy phase, which corresponds to the Fe–Ni NPs grown on the surfaces of the ND nanotemplates, (b) this phase has a Fe : Ni stoichiometry close to 1 : 3, which could correspond either to intermetallic $FeNi_3$ and/or to γ_2-taenite, (c) the development of graphitic-type layers encapsulating the Fe–Ni NPs is suggesting further diffusion of C atoms within the fcc alloy structure, and (d) a minor spinel oxide nanostructured phase could also be present in the samples.

To include the contribution of the Fe–Ni nanostructured phase in our fitting model we consider the relative literature on the analyses of the MS of $FeNi_3$. $FeNi_3$ or awaruite is considered as one of the two ordered phases encountered in the Fe–Ni system's phase diagram (the other being the $L1_0$ FeNi tetrataenite), which orders from the disordered state with very slow diffusion rates below 500 °C to form an ordered $AuCu_3$-type soft FM (γ'-fcc crystal $L1_2$) structure with a nominal iron-to-nickel atomic ratio of 1 : 3.[23,31,61] However, it is known that below the Curie temperature of 600 °C, the B_{hf} at the iron nuclei shows always a distribution around the B_{hf} value of the perfectly ordered $FeNi_3$ alloy, depending on the degree of Fe–Ni atomic order and/or on local stoichiometry contributions. Therefore, the existence of a distribution of B_{hf} values entails the presence of incomplete ordering and/or deviation of the nominal (Fe : Ni = 1 : 3) stoichiometry, leading to different surrounding configurations of the iron atoms as pointed out by J. W. Drijver *et al.*[61] In this work, J. W. Drijver *et al.* reported that a great determinant for understanding thoroughly the B_{hf} distribution observed in the nearly completely ordered $FeNi_3$ system is the relation of the B_{hf} with the local environment of the iron atoms around their first and second neighbouring shells, when these iron atoms occupy the nominal Fe crystallographic sites in the ordered structure.

Many scientists tried to study this effect in nearly completely ordered $FeNi_3$ alloys. In a typical perfectly ordered fcc $FeNi_3$ alloy, an iron atom is surrounded by twelve nickel atoms and zero iron atoms in the first neighbouring shell and by six iron atoms and zero nickel atoms in the second neighbouring shell. In terms of iron atom occupancy in these first and second neighbouring shells around the nominal Fe crystallographic sites of the $FeNi_3$ system, M. Kanashiro *et al.* used the notation

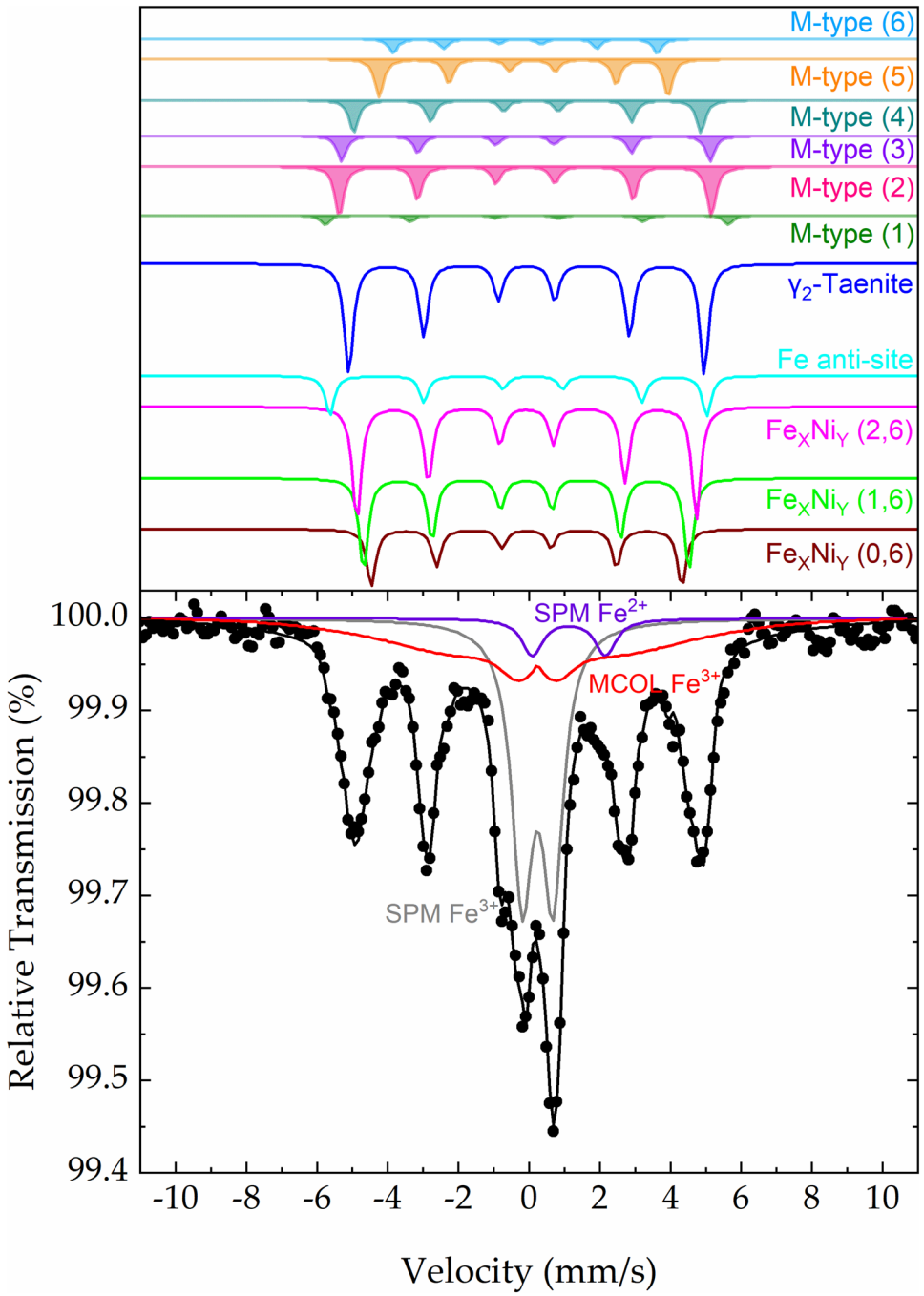

Fig. 6 ^{57}Fe Mössbauer fitted spectrum of the NHD-700C,30m sample collected at room temperature. Points represent the experimental data and the coloured lines the components used to fit the spectrum, with some of their base-lines shifted higher than 100% relative transmission to improve the clarity of this multicomponent fitting.

(n_1,n_2), where n_1 corresponds to the iron atom occupancy in the first neighbouring shell and n_2 to the iron atom occupancy in the second neighbouring shell.[62,63] Moreover, the probability of finding such configurations is given by eqn (1):

$$W(n_1) = \frac{12!}{(12-n_1)!n_1!}\left(\frac{3+\theta+S}{4}\right)^{12-n_1}\left(\frac{1-\theta-S}{4}\right)^{n_1} \quad (1)$$

where $\theta/4$ is the fractional deviation of the Fe concentration from the nominal Fe : Ni = 1 : 3 stoichiometry (Fe_XNi_Y, where $X = (1-\theta)/4$, $Y = (3+\theta)/4$ and $X + Y = 1$) and S is the long range order parameter defined as $S = 4/3(p - 1/4)$,[61] with p being the probability of finding an iron atom at the nominal Fe crystallographic sites of the ordered $FeNi_3$ system.

M. Kanashiro *et al.*[62,63] suggested that there are three main magnetically split contributions to be considered for analysing the MS of a nearly completely ordered Fe_XNi_Y alloy. Each one of these contributions corresponds to a different local atom

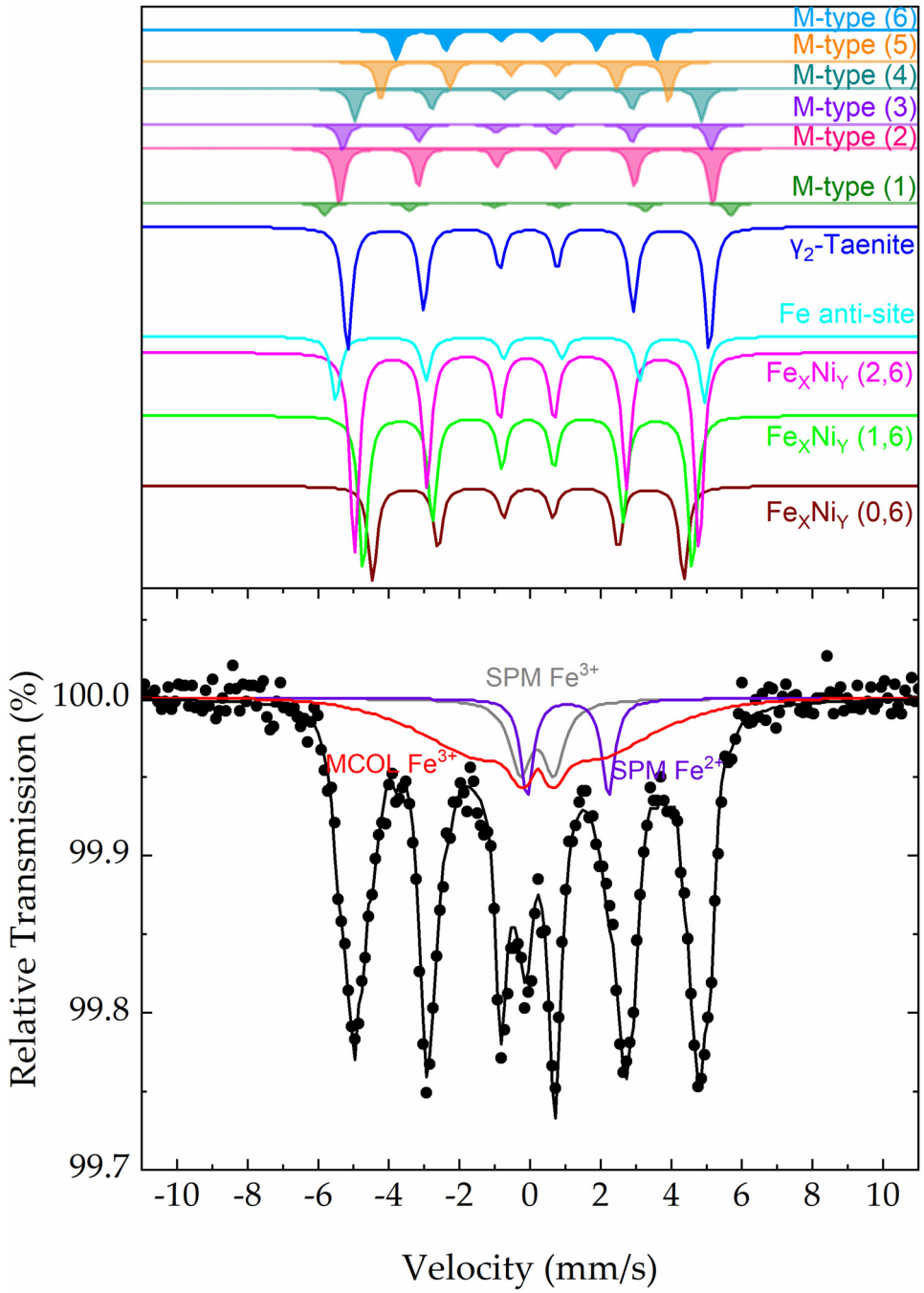

Fig. 7 ^{57}Fe Mössbauer fitted spectrum of the NHD-700C,4h sample collected at room temperature. Points represent the experimental data and the coloured lines the components used to fit the spectrum, with some of their base-lines shifted higher than 100% relative transmission to improve the clarity of this multicomponent fitting.

configuration (n_1,n_2) ascribed as (n_1,6), with n_1 ranging only from 0 to 2, namely (0,6), (1,6) and (2,6), since for $n_1 > 3$ all other configurations can be neglected due to vanishing $W(n_1)$ probabilities when the order parameter S is high enough to reach 0.7.

However, a subsequent study on this matter introduced by T. E. Cranshaw *et al.*,[64] highlighted the importance of considering also the occupancy of the iron atom located at the nominal nickel crystallographic site, thus forming an Fe anti-site configuration, as an additional and effective contribution to the interpretation of B_{hf} distribution in a nearly completely ordered $FeNi_3$ environment. More specifically, T. E. Cranshaw and his co-workers concluded that a systematic ordering of defects can be developed in both non-stoichiometric and disordered $FeNi_3$-type alloys, where apart from the statistically prominent iron sites Fe_XNi_Y (0,6), Fe_XNi_Y (1,6) and Fe_XNi_Y (2,6), an Fe anti-site configuration with equivalent statistical contribution, notated there as Fe_XNi_Y (4,0), should be included in the fitting model. The

Table 1 Mössbauer hyperfine parameters resulting from the best fits of the corresponding spectra of the samples shown in Fig. 5–7. IS is the isomer shift (given relative to α-Fe at 300 K), $\Gamma/2$ is the half-line width, QS is the quadrupole splitting, 2ε is the quadrupole shift, B_{hf}^{C} is the central value of the hyperfine magnetic field, ΔB_{hf} is the total spreading (Gaussian-type) of the B_{hf} values around the central B_{hf}^{C} value, and AA is the relative spectral absorption area of each component used to fit the spectra. Typical errors are ±0.02 mm s^{-1} for IS, $\Gamma/2$, 2ε and QS, ±3 kOe for B_{hf}^{C} and ±3% for AA

Sample	Components	IS (mm s^{-1})	$\Gamma/2$ (mm s^{-1})	Q.S. or 2ε (mm s^{-1})	B_{hf}^{C} (kOe)	ΔB_{hf} (kOe)	Area (%)	Color
AM-NHD precursor	SPM Fe^{3+} (1)	0.32	0.22	0.54	0	0	46	Dark cyan
	SPM Fe^{3+} (2)	0.34	0.25	1.04	0	0	54	Purple
NHD-700C,30m	Fe_XNi_Y (0,6)	0.03	0.15	0.00	273	0	5	Maroon
	Fe_XNi_Y (1,6)	0.02	0.15	0.00	286	0	8	Green
	Fe_XNi_Y (2,6)	0.03	0.15	0.00	298	0	9	Magenta
	Fe anti-site	0.00	0.15	−0.41	331	0	3	Cyan
	γ_2-Taenite	0.03	0.15	0.00	312	0	7	Blue
	M-type (1)	0.04	0.15	0.01	354	0	2	Olive
	M-type (2)	0.00	0.15	0.00	327	0	4	Pink
	M-type (3)	0.00	0.15	0.04	324	0	3	Purple
	M-type (4)	0.11	0.15	−0.11	305	0	3	Dark cyan
	M-type (5)	0.08	0.15	−0.25	254	0	3	Orange
	M-type (6)	−0.07	0.15	0.13	232	0	1	Light blue
	SPM Fe^{3+}	0.34	0.36	0.87	0	0	28	Grey
	SPM Fe^{2+}	1.23	0.36	2.06	0	0	4	Dark purple
	MCOL Fe^{3+}	0.34	0.15	0.00	174	179	21	Red
NHD-700C,4h	Fe_XNi_Y (0,6)	0.05	0.15	0.00	274	0	7	Maroon
	Fe_XNi_Y (1,6)	0.04	0.15	0.00	290	0	12	Green
	Fe_XNi_Y (2,6)	0.01	0.15	0.00	303	0	14	Magenta
	Fe anti-site	0.00	0.15	−0.36	324	0	5	Cyan
	γ_2-Taenite	0.06	0.15	0.00	318	0	10	Blue
	M-type (1)	0.04	0.15	0.01	357	0	1	Olive
	M-type (2)	0.00	0.15	0.00	328	0	5	Pink
	M-type (3)	0.00	0.15	0.04	324	0	2	Purple
	M-type (4)	0.11	0.15	−0.11	305	0	3	Dark cyan
	M-type (5)	0.08	0.15	−0.25	253	0	3	Orange
	M-type (6)	−0.07	0.15	0.13	229	0	2	Light blue
	SPM Fe^{3+}	0.31	0.36	0.95	0	0	8	Grey
	SPM Fe^{2+}	1.17	0.22	2.31	0	0	6	Dark purple
	MCOL Fe^{3+}	0.33	0.15	0.00	147	116	22	Red

notation Fe_XNi_Y (4,0) to describe the Fe anti-site configuration is given by T. E. Cranshaw *et al.* due to its identical environment with an Fe atom located at a nominal Fe crystallographic site that has 4 Fe anti-site atoms on the first neighbouring shell and 6 Ni anti-site atoms on the second neighbouring shell.

To this extent and to elucidate the B_{hf} distribution phenomena contributing to the appearance of a resonant line broadening in the spectra of our annealed samples, which most probably might be the actual situation, we conveniently accept M. Kanashiro's and T. E. Cranshaw's arguments. Therefore, we use the notations Fe_XNi_Y (0,6), Fe_XNi_Y (1,6), Fe_XNi_Y (2,6) and Fe anti-site, corresponding to a set of four components coloured maroon, green, magenta and cyan respectively, to model the contribution of the Fe_XNi_Y phase in our spectra shown in Fig. 6 and 7.

Accepting an average Fe_XNi_Y stoichiometry of Fe : Ni = 0.34 : 0.66 as indicated by TEM for the NHD-700C,4h sample, from the definition of the fractional deviation of the Fe concentration from the nominal Fe : Ni = 0.25 : 0.75 (1 : 3) stoichiometry in eqn (2):

$$\frac{\mathrm{Fe}}{\mathrm{Ni}} = \frac{0.34}{0.66} = \frac{\frac{1-\theta}{4}}{\frac{3+\theta}{4}} \quad (2)$$

we can calculate θ to be −0.36. Furthermore, the probability $1 - p = W_{Fe,w}$ of finding an Fe anti-site atom in such a $Fe_{0.34}Ni_{0.66}$ alloy is given by eqn (3):[63]

$$W_{Fe,w} = (1 - \theta - S)/4(1 - \theta). \quad (3)$$

This probability is equal to the ratio of the absorption area (AA) of the Fe anti-site component relative to the total AA of all components describing this phase in the NHD-700C,4h sample spectrum. This ratio is ∼0.13 (5%/38%), which together with θ = −0.36 leads to estimating the order parameter value for the $Fe_{0.34}Ni_{0.66}$ alloy phase in the NHD-700C,4h sample to be $S \approx 0.67$. A similar ratio of 0.12 (3%/25%) is found for the corresponding components of the NHD-700C,30m sample spectrum.

This set of components provide AA to cover the characteristic contributions (i) of the MS, but, on the other hand, it is not the only case of an Fe–Ni fcc phase that can do so. This is because the fcc FM disordered γ_2-taenite (nickel-rich) Fe–Ni phase, whose presence is more prominent in the range of 500 to 650 °C according to the Fe–Ni phase diagram,[65,66] modelled by a single magnetically split component, can also supply AA to cover this characteristic contributions (i).[23,67] Consequently, we must consider this component as well in our fitting model. This component is coloured blue in Fig. 6 and 7.

We now turn our attention to the satellite contributions (ii) of the MS. For this part of the spectra, we take into account the TEM analyses which show the development of graphitic-type layers surrounding the Fe–Ni NPs and suggest further the diffusion of carbon atoms at interstitial sites in their structure. This pattern has been found to exist almost identically in the similar Fe–Co NPs/ND NHD system developed and studied recently by our group.[49] There, this part was attributed to iron atoms arranged on a non-extensive martensitic-type Fe–Co phase formed in the interface between the Fe–Co NPs and the developed graphitic-type layers surrounding them. Following the similarity of the TEM and Mössbauer spectroscopy experimental data observed for these two iron-based binary alloy NHD systems, we attribute the satellite contributions (ii) of the current MS to a martensitic-type Fe–Ni phase formed within the Fe–Ni NPs, in the interface between them and the supporting ND nanotemplate growth platforms.

We utilized six minor magnetically split components for this purpose, which correspond to iron atoms exhibiting a metallic alloy character while also being influenced by an adjacent neighbouring carbon atom in their immediate vicinity.[13] Based on detailed analyses of the structural properties and related MPs of these iron sites within the martensite structure as reported in the literature,[68–75] we can assign specific atomic environments to these components that model the satellite contributions (ii). Specifically, component M-type (1), shown in olive in Fig. 6 and 7, has the highest B_{hf} value and represents iron atoms in dilated Fe–Ni crystal lattice positions far from interstitial carbon atoms. Component M-type (2), depicted pink in Fig. 6 and 7, corresponds to iron atoms that are distant third neighbours to interstitial carbon atoms, slightly influenced by their presence. Components M-type (3) and M-type (4), shown in purple and dark cyan in Fig. 6 and 7, respectively, represent iron atoms in the closest second- and first-neighbour positions to interstitial carbon atoms. Lastly, components M-type (5) and M-type (6), shown in orange and light blue in Fig. 6 and 7, respectively, have the lowest B_{hf} values and are associated with Fe atoms that have two nearest-neighbour carbon atoms. These environments, with two interstitial carbon atoms as nearest neighbours, are more likely to exist at higher carbon concentrations according to relative binomial distribution models.[71–73,76,77]

Subsequently, the central part (iii) of the MS is fitted with two quadrupole split components and one very broad magnetically split component with collapsing B_{hf} characteristics, all having ionic Fe character. In the cases of the collapsing B_{hf} components, a Gaussian-type spreading ΔB_{hf}[78] of their B_{hf} values around the central B_{hf}^{C} value was allowed to cover the line broadening at this part of the MS.

Assembling in the fitting model the components corresponding to the three sets of contributions for the annealed samples' MS described above, we got back quite adequate fitting results. The resulting MPs values of all components are listed in Table 1. The MPs values of Fe_XNi_Y and γ_2-taenite are very close to those found in the literature for these phases.[23,62–64,67] The same holds also for the set of components used to fit the martensitic-type Fe–Ni phase.[68–75] Regarding the set of components used to fit the contribution (iii) of the MS, we observe that their MPs values correspond to high-spin Fe^{3+} and Fe^{2+} ion sites in oxygen first-neighbour environments, indicating the presence of a spinel oxide phase with some additional Fe^{2+} ions in its structure,[52] which experiences fast SPM relaxation phenomena similar to those found at the precursor sample. From these results, it is evident that the existence of the quadrupole split contributions (iii) in the annealed samples is remnant of the main SPM spinel oxide contributions observed in the precursor sample, most probably because of incomplete oxide-to-alloy reduction reactions.

The resulting MPs values of the set of components corresponding to the Fe_XNi_Y, γ_2-taenite, martensitic-type Fe–Ni and spinel oxide phases are very similar for the two annealed samples. This finding emphasizes the high resemblance and iterability of all phases developed in these samples, verified also by the XRD and TEM results. However, a significant change is observed for the total AA value found for the components describing the spinel oxide phase. In particular, this value drops from 53% for the NHD-700C,30m sample to 36% for the NHD-700C,4h sample. In contrast, the total AA values for the components of the Fe_XNi_Y and γ_2-taenite phases increase from 25% to 38% and from 7% to 10% respectively for these samples. On the other hand, the sum of the AA values for the components of the martensitic-type Fe–Ni phase remains constant in both samples. These findings indicate that the sample with longer annealing duration contains relatively higher amounts of the fcc Fe–Ni phases and lower amounts of the spinel oxide phase. Thus, increasing the annealing time seems to favour the formation of the fcc Fe–Ni phases as a result of the reduction of the spinel oxide seeds emerging from the precursor sample. Based on these AA values, we can deduce a 'conversion efficiency factor' from the spinel oxide precursor seed phase to all the Fe–Ni alloy related phases found in our annealed samples, defined as the sum of their AAs, since the rest of the AAs represent the residual spinel oxide phase in the annealed samples. This factor increases from 47% to 64% as the annealing duration increases from 30 min to 4 h. It can thus be suggested that the magnitude of the annealing duration has a beneficial effect on the conversion of the spinel oxide precursor phase to the Fe–Ni alloy phase. However, other factors such as the particle size of the spinel oxide seeds, as well as the availability and proximity of the sp^2-type carbon atoms, could also be of similar importance.

To verify the accuracy and consistency of our fitting model, we inspected the thermal evolution of the MS at 77 K (see Fig. S3, ESI†). The features of these spectra are very similar to those found for the RT MS. Consequently, the 77 K MS can be fitted with the same fitting model as that used for the RT spectra. The resulting MPs values are listed in the ESI,† Table S2. We observe that all components acquire the expected shifts in their isomer shift (IS), qudrupole splitting (QS), quadrupole shift (2ε) and B_{hf} values due to the temperature drop, while the sum of the AA values for the components of each phase is very similar (within the expected errors) to those found

at RT. The only difference refers to the individual AA values for the components of the spinel oxide phase. In particular, the AA value of the MCOL Fe^{3+} component increases at the expense of the AA value of the SPM Fe^{3+} component, relative to those found at the RT MS. This denotes an increase in the characteristic SPM relaxation time τ for a part of the SPM spinel oxide NPs, which are becoming magnetically blocked at 77 K.[47,52,59,60]

2.4 Magnetization and magnetic susceptibility

The magnetic properties of the AM-NHD precursor and the annealed NHD samples are further characterized by their magnetization (M) *versus* (*vs.*) applied magnetic field (H) under constant temperature and magnetic susceptibility (χ_g) *vs.* temperature (T) under constant H measurements. The magnetic measurements of the AM-NHD precursor are shown in the ESI,† Fig. S4 and S5, while those of the annealed NHD samples appear in Fig. 8 and 9, respectively. These measurements reveal the magnetic behaviour, determined by the relative compositions, type of nanostructures as well the magnetic interactions and interconnections of the NPs present in the AM-NHD precursor and the NHD annealed samples.

In particular, the M *vs.* H isothermal loops of the AM-NHD precursor in Fig. S4 (ESI†) present a clear linear behaviour at 400 K and 300 K, while at 2 K a sigmoidal curve develops which however possesses linear behaviour at high H values, lack of saturation and a coercivity of about 300 Oe. These characteristics correspond to an assembly of very small spinel oxide ferrimagnetic NP seeds, which are so small that in their entirety experience very fast SPM relaxation at high temperatures. As the temperature decreases, the rate of the SPM relaxation reduces for a part of this assembly, most probably for those larger in size and more interconnected to each other on the surfaces of the ND nanotemplates, which gradually become magnetically blocked, while the rest of the smaller spinel oxide NPs still experience very fast SPM relaxation even at temperatures as low as 2 K. These characteristics are further confirmed by the χ_g *vs.* T measurements in Fig. S5 (ESI†), where at the low applied field of 99 Oe the ZFC branch presents an initial fast drop in χ_g values as the temperature increases at low temperatures, followed by general stabilization and gradual lowering of these values at higher temperatures, interrupted only by two small and broad local maxima at around 180 K and 225 K. For the corresponding FC branch, the increase in χ_g is smoother as the temperature decreases, which is an expected behavior from the effect that the applied field imposes on the whole assembly of the SPM spinel oxide NPs in the cooling mode. The two branches in this applied field (99 Oe) bifurcate below ~350 K. By increasing the applied field to 999 Oe the FC and ZFC branches coincide in a larger temperature region and bifurcate only below ~70 K, a behavior again expected for such a SPM NP system with a relatively narrow particle size distribution and weak to vanishing interparticle interactions under the effect of a higher applied field. All these characteristics come in perfect agreement with the corresponding characteristics deduced from the Mössbauer spectroscopy measurements at different temperatures on the AM-NHD precursor, confirming the very fast SPM relaxation and the effect of temperature on it revealed by this method.

The M *vs.* H isothermal loops of NHD-700C,30m and NHD-700C,4h annealed samples recorded at 400, 300 and 2 K show clear FM characteristics with hysteresis, exhibiting coercivities that range from about 10 to about 600 Oe depending on temperature (see Table 2). These characteristics are accompanied, however, by constant and non-vanishing dM/dH slopes at high H values at all temperatures. These slopes denote a SPM contribution that can be attributed to the spinel oxide NPs found to be present in these annealed samples, which, due to their very small particle size, experience very fast SPM relaxation at all temperatures. Typical soft FM Fe–Ni alloys present M_S values that reach 125 emu g^{-1} and coercivities of about 35 to

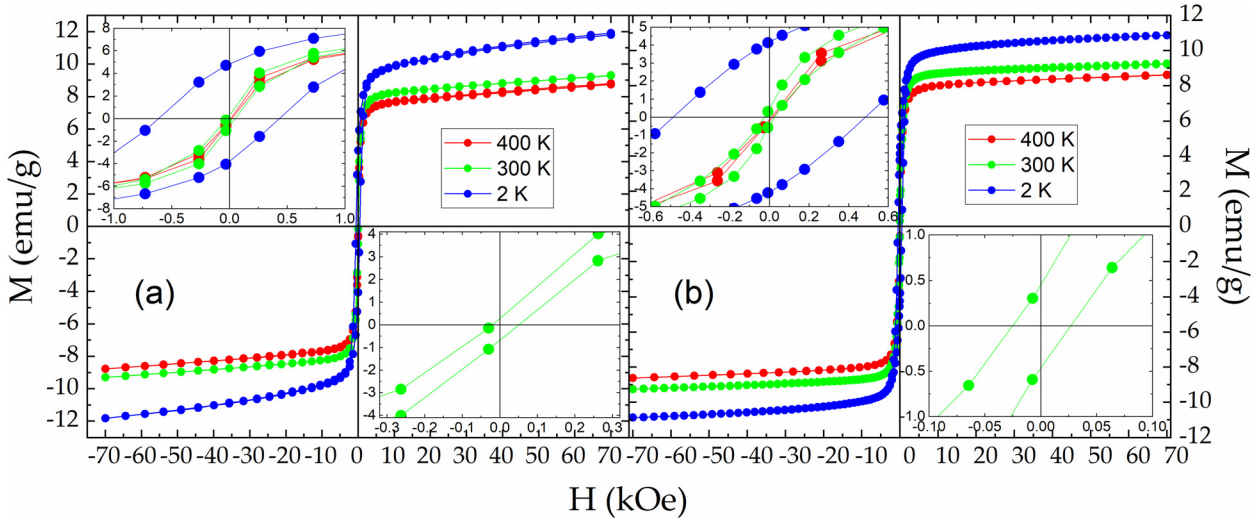

Fig. 8 Magnetization *vs.* applied magnetic field isothermal loops of the NHD-700C,30m (a) and En-NHD-700C,4h (b) samples measured at different temperatures indicated by different colours. The insets in each set of measurements show the details of the loops' characteristics around zero applied magnetic field for all temperatures (upper left) and with even more detail for the 300 K loop (lower right).

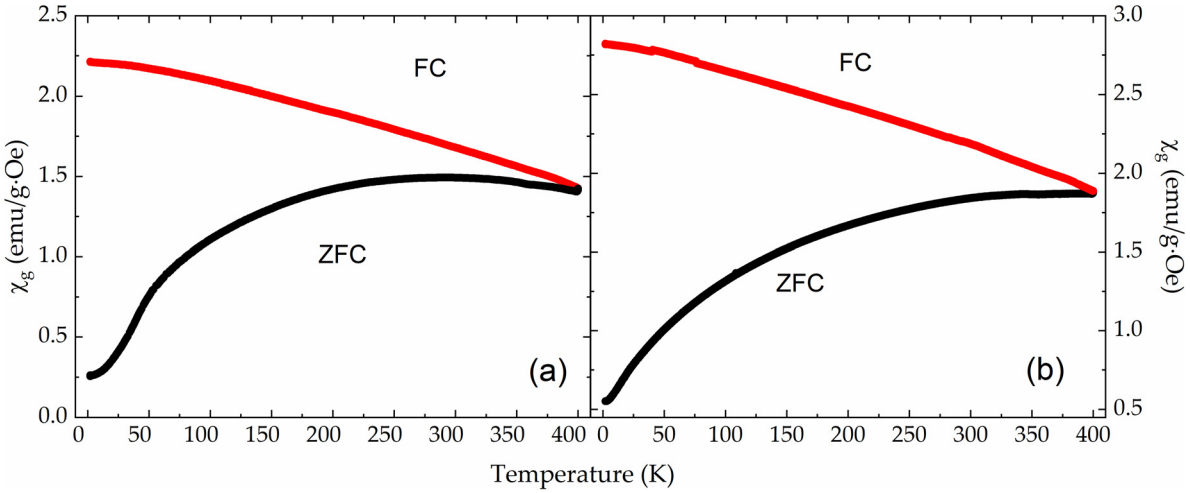

Fig. 9 Magnetic susceptibility *vs.* temperature measurements of the NHD-700C,30m (a) and NHD-700C,4h (b) samples conducted under an applied field of 99 Oe.

60 Oe at RT.[65,79–81] It is evident that the maximum M values found in our samples are in the range of 10% of the M_S values of the soft FM Fe–Ni alloys, and this can be justified by the fact that we have scheduled a 10 wt% of Fe, Ni metals loading in our synthesis. Furthermore, the large increase in the coercive fields from 300 K to 2 K indicates that the assembly of Fe–Ni FM NPs should also experience SPM relaxation, which gradually changes its characteristic relaxation time as T decreases.[59,82]

The χ_g *vs.* T measurements of both samples, recorded under an applied field of 99 Oe, are shown in Fig. 9 and reflect the main SPM relaxation features of the FM NPs. In both diagrams, the χ_g values of the ZFC branches monotonically increase as T increases, with no local maxima up to 400 K, while the FC branches are much smoother and continuously rise as T decreases. The two branches coincide only at the highest measured temperature point of 400 K for both samples, suggesting a relative broad size distribution for the magnetically ordered nanophases involved in these samples.

These results reflect a system, whose magnetic behaviour is clearly influenced by the larger in size and/or more strongly magnetically interacting metallic Fe–Ni NPs, which are magnetically blocked even at 400 K, as delineated by the presence of small hysteresis in the M *vs.* H loops.[59]

Similar behaviours are obtained in the χ_g *vs.* T measurements of both annealed samples recorded under an applied field of 999 Oe (Fig. S6, ESI†). There, however, the ZFC branches display a minor local maximum around 167 K and 147 K for the NHD-700C,30m and NHD-700C,4h sample respectively, suggesting a slight diversification in the SPM relaxation behaviour for different assemblies of magnetic NPs originating from the differences in NP size distribution, which can be revealed by the higher H values in these measurements.[82] Moreover, the differences in the Fe–Ni and spinel oxide NP content in each sample could also justify the slightly higher maximum χ_g values observed for the NHD-700C,4h sample relative to those found for the NHD-700C,30m sample. As the nominal M values are higher for the Fe–Ni phase relative to those of the spinel oxide phase,[83] the higher amount of spinel oxide NPs evident by the ^{57}Fe Mössbauer spectroscopy measurements for the NHD-700C,30m sample should contribute to its reduced χ_g values relative to those found for the NHD-700C,4h sample at relatively low fields (up to 1 kOe). On the other hand, as the SPM contribution to the total M values for the spinel oxide phase is higher at high fields ($>$10 kOe), the characteristics of the M *vs.* H isothermal loops are influenced significantly by this contribution at these fields, as evident by the higher dM/dH slope and maximum M values recorded for the NHD-700C,30m sample in comparison to the NHD-700C,4h sample (Fig. 8, Table 2). Finally, the average coercivity values are comparable between the two annealed samples at all measured temperatures, but for the NHD-700C,4h sample they are more symmetric regarding the individual H_{C+} and H_{C-} values compared to those of the NHD-700C,30m sample, which is an effect that can be

Table 2 Magnetic characteristics derived from the isothermal loops of Fig. 8

Sample	T (K)	M_{max+} (emu g^{-1})	M_{max-} (emu g^{-1})	M_{R+} (emu g^{-1})	M_{R-} (emu g^{-1})	H_{C+} (Oe)	H_{C-} (Oe)
NHD-700,30m	400	8.8	−8.8	−0.1	−0.2	21	10
	300	9.3	−9.3	0.3	−0.6	50	−21
	2	11.9	−11.8	4.8	−3.8	433	−611
NHD-700,4h	400	8.6	−8.6	−0.1	−0.2	18	9
	300	9.2	−9.2	0.4	−0.5	27	−25
	2	10.9	−10.9	4.1	−4.2	487	−488

attributed again to the lower amount of the residual spinel oxide phase contained in the former sample, where the magnetic properties of the main FM Fe–Ni phases dominate, relatively free from the exchange bias effects that the residual spinel oxide phase can contribute.

2.5 Discussion

Summarizing the results and interpretation of all the experimental techniques employed in this work, the interconnection between the developed phases in the precursor, as well as in the annealed samples and their properties, should be elaborated thoroughly to extract the appropriate conclusions. From the results it has become evident that the AM-NHD precursor, which is composed of SPM spinel oxide NP seeds developed on the ND nanotemplates, influences fundamentally the properties of the final annealed samples. On the other hand, the structure and morphology of the ND NPs forming the nanotemplates, which are created through detonation explosions, are equally critical both for the initial growth and anchoring of these spinel oxide NP seeds at the impregnation step, as well as for the development of the Fe–Ni NPs during the final annealing step of the synthesis.

It is known that the initial process drives specific mechanisms observed in similar systems of ND substrates,[46,49] which involve blending and interaction among these nanostructures. In particular, the native presence of carboxyl/hydroxyl functional groups on the ND NP surfaces in the moist mixture at the initial impregnation process facilitates strong attractive interactions with the dissolved metallic salts, due to the hygroscopic nature of the salts and the hydrophilic functional groups on the NDs.[10] These interactions lead to the formation of strong coupling between the Fe^{3+} and Ni^{2+} ions and the functional groups, resulting in their firm attachment on the NDs' surfaces, by the formation of (i) iron-oxide–carbon and nickel-oxide–carbon and (ii) direct iron–carbon and nickel–carbon bonds.[3,12]

Furthermore, the thermal treatment of the precursor sample in vacuum-evacuated quartz ampoules at high temperatures triggers the involvement of strong reducing agents in this second step of the synthesis of the final nanohybrid samples. These agents are the sp^2-coupled carbon atoms existing already as native species at the surfaces of the ND NPs and are further developed during thermal annealing in close proximity to the growing metallic nanoparticles.[3,11,84,85] These sp^2-hybridized carbon atoms, along with the low O_2 pressure due to the vacuum existing inside the ampules (10^{-3} Torr), provide the appropriate conditions for the full reduction of the AM-NHD' Fe^{3+} and Ni^{2+} ions in the spinel oxide NPs to the Fe^0 and Ni^0 atoms that form the Fe–Ni alloy NPs. Moreover, TEM observations verified that the native sp^2 carbon atoms are assembled into graphitic-type layered nanostructures that are encapsulating the metallic NPs partially or in total. Their supply and further development are proposed to emerge from the ND sp^3 cores, as the later undergo a surface graphitization procedure at elevated temperatures of 700 °C and above. This process is known to be further enhanced by the presence of defects, such as carbon atom vacancies and dislocations, as well as by the presence of metallic elements like iron, cobalt and nickel on the surfaces of the ND NPs that can act as catalysts and therefore can facilitate the rearrangement of carbon atoms into graphitic-type structures.[3,13,86] Thus, carbon atoms initially participate in the formation and further development of the Fe–Ni NPs through their reduction capacity, while in sequence the Fe–Ni NPs can mutually serve as nucleation centres for the initiation and further construction of graphitic-type layers on their surfaces, as evidenced by HRTEM. Moreover, the graphitization process of these layers leads to low binding energies for the sp^2-type carbon atoms, inducing their further lateral diffusion within the structure of the Fe–Ni NPs. Therefore, high temperatures combined with the NDs' morphology appear not only to promote the formation of Fe–Ni NPs, but also to favour a partial lateral diffusion of carbon atoms in the regions across the interfaces between the metallic NPs and ND NPs, where the source of carbon atom is originating. We propose that this diffusion mechanism is responsible for the development of the minor tetragonally distorted martensitic-type Fe–Ni phase that has non-extensive characteristics, in the sense that its appearance in the Fe–Ni NPs is related to the presence of the adjacent ND NPs. We support this proposal to the evidence provided by ^{57}Fe Mössbauer spectroscopy, which is an atomic-level probe technique, while XRD, TEM and magnetization measurements, being more collective and due to the high similarity of the fcc and martensitic-type Fe–Ni crystal structures provide their average characteristics, which cannot distinguish clearly these two phases.

Another issue that needs further clarification refers to the fcc Fe–Ni phases present in the NHD annealed samples. The results indicate that two closely related phases regarding their structural and magnetic properties, namely γ' Fe_XNi_Y with $X:Y \approx 1:3$ and γ_2-taenite, are developed that can be distinguished only by ^{57}Fe Mössbauer spectroscopy. TEM observations and EDS measurements suggest that both iron-alloy based phases are rich in the second alloying element (Ni), without however distinguishing between the two phases. On the other hand, the presence of the residual SPM spinel oxide phase with a $NiFe_2O_4$ stoichiometry in both annealed samples indicates that a portion of the total iron contained in the system appears as Fe^{3+} ions in this Ni poor spinel oxide phase. This could justify the average Ni rich stoichiometry of the Fe–Ni alloy system ($Fe_{0.36}Ni_{0.64}$) relative to the nominal equiatomic stoichiometry considered in the synthesis, by accepting that the amount of iron missing in the alloy phase is located in the oxide phase.

Consequently, the combination of these synthesis steps, as well as the internal mechanisms that are accompanying them, leads to the development of a unique hybrid metallic compound system. However, as we mentioned earlier, similar characteristics have been found in the study of the Fe–Co/NDs system, leading to the formation of a recurring morphological pattern for these two systems. One could easily relate the repetitiveness of these characteristics to the step-by-step routine synthesis that both systems share. Therefore, it would be

expected to see the formation of metallic NPs on the surfaces of ND NPs, as well as the formation of graphitic-type layered nanostructures at the interface between the metallic and ND NPs, as this is directly related to the graphitization process of native sp^2-type carbon atoms existing on the surfaces of ND NPs at high temperatures. This process is favoured by the presence of similar metallic elements used in the two systems.

Additionally, the appearance of the martensitic-type phase in these systems should be expected, as this is favoured during the graphitization process in the second part of the synthesis procedure. This is proposed because from the above results we understand that the configuration of the morphological environment that includes the interconnected martensitic-type and graphitic-type-layered phases of the two iron alloy systems (Fe–Ni and Fe–Co) is determined by the actions of both the ND NPs and the second element of the iron-based alloy, whose presence seems to be catalytic in this respect. To understand these arguments, it is important to consider some other very significant aspects that the presence of the martensitic-type phase and the absence of other related phases indicate.

According to the literature, the appearance of martensitic-type phases could be observed when the concentration of carbon atoms in the iron alloy is relatively small and does not exceed 2–5 at%. In this way, one could say that on the one hand the strong affinity of the carbon atoms to form direct bonds easier with iron atoms than with cobalt and nickel atoms,[87] and on the other hand the affinity of the formation of stronger metallic bonds between iron and the second metallic element in the two alloy systems (Ni and Co), can lead to the avoidance of the establishment of direct bonds between the carbon atoms and the metallic elements. These bonds favour the formation of either iron or iron–nickel or iron–cobalt carbides,[88–92] which are phases that we have not observed in any of these two iron alloy systems. We propose that this mechanism leads to the conservation of the alloyed crystal structure for the metallic NPs with the retainment of the carbon atoms at the interstitial sites, where their presence constitutes the configuration of the martensitic-type phase. This conclusion is further confirmed by considering the situation where the second element of the iron alloy in the NHD system is absent. In this case the developed NHD composite material at the second step of the synthesis procedure should be related to the reduction of only iron spinel oxide NP seeds in the precursor during the annealing process. This synthesis and study of the resulting material have already been done following the same procedures at similarly high temperatures (750 °C, 4 h), and the results showed the formation of only one nanostructured iron carbide (Fe_3C) phase.[47] There, it was concluded that the iron carbide formation resulted from the direct interaction of a significant portion of the sp^2-type carbon atoms with the reduced part of metallic iron. Thus, under certain synthesis conditions, iron alone, and not alloyed with Co or Ni, led to the direct formation of iron carbide upon interaction with carbon atoms, rather than the formation of iron alloy NPs containing the martensitic-type phase. This is driven most probably by the easier and faster diffusion of the carbon atoms within the pure iron structure than the iron alloyed with Ni or Co structures[93–95] and highlights the significance of the presence of the second metallic element in these iron-based binary alloy systems for the formation of the martensitic-type phase.

3. Conclusions

In this study, we have successfully synthesized a novel magnetic nanohybrid material by growing FM fcc Fe–Ni NPs on ND nanotemplates, using a two-step preparation procedure combining wet chemical methods and annealing under controlled conditions. These Fe–Ni NPs, with an average size of 10 nm, are uniformly distributed on the surface of the ND nanotemplates, exhibiting a nickel-rich concentration (approximately 64 at% Ni), attributed to a mixture of awaruite ($FeNi_3$) and γ_2-taenite phases that display FM behaviour over a temperature range spanning from 2 K to 400 K, with coercivity values increasing from $\sim$10 Oe at 400 K to $\sim$610 Oe at 2 K. The formation of the predominant fcc Fe–Ni phases is consistently accompanied by a secondary non-extensive tetragonally distorted martensitic-type Fe–Ni phase.

Particularly, the development of this unique martensitic-type Fe–Ni phase is attributed to the distinctive morphological properties of the NDs growth matrices, which enable and facilitate the formation of carbon sp^2-type nanostructures at the surfaces of the Fe–Ni NPs during the annealing procedure in the second step of the synthesis. These graphitic-type layered nanostructures, which appear to enshroud the metallic Fe–Ni NPs grown on the surfaces of the NDs, provide an ideal environment for interstitial carbon atom diffusion within the Fe–Ni lattices at elevated temperatures, which consequently trigger the non-extensive formation of the Fe–Ni martensitic-type configurations.

These findings further broaden the understanding of the iron alloy-based nanohybrid magnetic systems and highlight the essential and catalytic role of the ND NPs in the development of unique magnetic phases, such as these magnetic metallic NPs that embed a combination of FM cubic and tetragonally distorted martensitic-type phases. The intentions of this work are to unveil and highlight the mechanisms responsible for the development of these unique hybrid magnetic nanostructures and to create a fertile ground for the further development and study of similar systems.

4. Experimental

4.1 Materials synthesis

The synthetic route elaborated for the synthesis of hybrid magnetic crystalline Fe–Ni/ND nanostructures involved a two-step procedure (Fig. 10): initially, a wet chemistry impregnation step[10,96] aimed for the delivery of an as-made (AM) chemical precursor, followed by a thermal treatment of the AM precursor under controlled conditions. A nominal Fe : Ni atomic ratio of 1 : 1 was implemented, using the appropriate amounts of the corresponding metal salts.

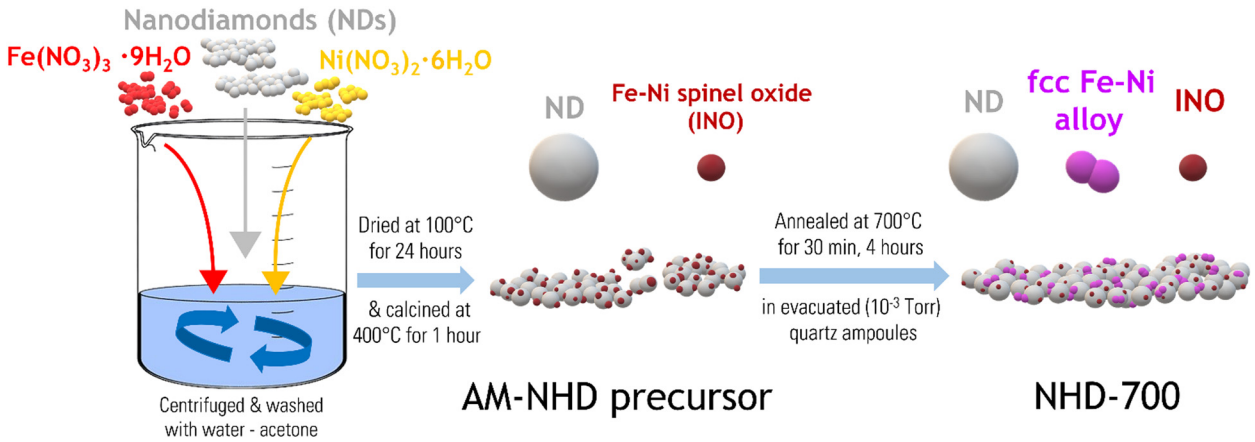

Fig. 10 Graphical representation of the two-step synthesis procedure of the as-made nanohybrid (AM-NHD) chemical precursor and the final annealed nanohybrid samples (NHD-700).

A total ~10 wt% of combined Fe and Ni metal to the ND mass ratio was considered for the preparation of the corresponding AM nanohybrid (AM-NHD) precursor sample.

In particular, for the AM-NHD precursor, 35 mg of $Fe(NO_3)_3 \cdot 9H_2O$ (99.99+%, Aldrich 254223-50G) and 25 mg of $Ni(NO_3)_2 \cdot 6H_2O$ (>99.99+%, Aldrich 13478-00-7) were dissolved in 0.5 mL of deionized water. The solution was then mixed with 90 mg of detonation ND powder (98%, Aldrich 636428-1G). The mass concentrations of all components were calculated to ensure that the final AM hybrid precursor contained ~10 wt% of equiatomic Fe and Ni metal percentage. The mixture was blended and homogenized in a moist paste form using an agate mortar and pestle and then allowed to dry at 100 °C for 24 h. After dehydration, the material was re-homogenized into a fine powder and calcined in air at 400 °C for 1 h. This process aimed to remove the unwanted nitrates and produce uniform well dispersed iron–nickel oxide (INO) NP seeds on the surfaces of the ND nanotemplates (see Fig. 10). Afterwards, thermal treatment of the AM-NHD precursor was conducted in sealed under vacuum (10^{-3} Torr) quartz ampoules at temperatures of 700 °C for varying time intervals of 30 min (NHD-700C,30m sample) and 4 h (NHD-700C,4h sample).

4.2 Materials characterization

Characterization and study of the structural and morphological properties, stoichiometry, and particle size of the prepared samples were carried out by powder XRD, using Cu Ka radiation on a Bruker Advance D8 diffractometer and analytical TEM/STEM observations, which were carried out using a 200 kV JEOL JEM F200 TEM/STEM microscope equipped with a cold field emission gun (CFEG) and an OXFORD X-Max 65T EDS detector. Prior to TEM observations, the samples were dispersed in ethanol and suspended in ultrasound for up to 40 minutes, while a single drop of very dilute suspension of each sample was placed on a carbon-coated Cu grid and left to dry naturally by evaporation under ambient conditions. Inquiries of the samples' magnetic properties were performed on a conventional vibrating sample magnetometer (VSM) (LakeShore 7300) and a VSM equipped magnetic property measurement system (Quantum Design, MPMS 3) through mass magnetization M and χ_g measurements. The M *vs.* H hysteresis loops were collected at constant temperatures of 2, 300, and 400 K at fields up to 70 kOe. The ZFC and FC χ_g *vs.* T curves were recorded upon warming the samples in the temperature range of 2 to 400 K at two different H values of 99 and 999 Oe, after cooling them at zero H, and upon cooling, directly after the warming procedure under the above H fields, respectively. To investigate in detail the iron-bearing phases' electronic, magnetic, structural, and morphological properties, ^{57}Fe Mössbauer spectra (MS) were collected in transmission geometry at sample temperatures of 300 and 77 K, using constant-acceleration spectrometers, equipped with ^{57}Co(Rh) sources kept at RT, in combination with a liquid N_2 bath (Oxford Instruments Variox 760) Mössbauer cryostat. For the velocity calibration of the spectrometers metallic α-Fe at RT was used, and all isomer shift values were given relative to this standard. The recorded MS were fitted and analysed using the IMSG code.[78]

Author contributions

Conceptualization: A. P. D. and P. G. Z.; methodology: A. P. D., P. G. Z., and A. B. B.; software: A. P. D.; validation: A. P. D., P. G. Z., A. B. B., and G. P. D.; formal analysis: A. P. D., P. G. Z., P. C., and G. P. D.; investigation: P. G. Z., A. B. B., P. C., G. P. D., and A. P. D.; resources: P. G. Z., A. B. B., P. C., G. P. D., A. M., and A. P. D.; data curation: P. G. Z., A. B. B., P. C., G. P. D., and A. P. D.; writing – original draft preparation: P. G. Z. and A. P. D.; writing – review and editing: P. G. Z., P. C., G. P. D., and A. P. D.; visualization: P. G. Z. and A. P. D.; supervision: A. P. D.; project administration: A. P. D.; funding acquisition: A. P. D. All authors have read and agreed to the published version of the manuscript.

Conflicts of interest

The authors declare no conflict of interest.

Data availability

The data supporting this article are available within the article and as part of the ESI.†

Acknowledgements

P. G. Z. acknowledges the support of this research work by the Hellenic Foundation for Research and Innovation (HFRI) under the 3rd Call for HFRI PhD Fellowships (Fellowship Number: 06623). The use of the XRD and VSM Laboratory Network Units of the University of Ioannina is gratefully acknowledged.

References

1 *Functional Hybrid Materials*, ed. P. Gómez-Romero and C. Sanchez, Wiley, 1st edn, 2003, DOI: 10.1002/3527602372.
2 P. Gomez-Romero, A. Pokhriyal, D. Rueda-García, L. N. Bengoa and R. M. González-Gil, Hybrid Materials: A Metareview, *Chem. Mater.*, 2024, **36**(1), 8–27, DOI: 10.1021/acs.chemmater.3c01878.
3 X. Duan, *et al.*, sp^2/sp^3 Framework from Diamond Nanocrystals: A Key Bridge of Carbonaceous Structure to Carbocatalysis, *ACS Catal.*, 2019, **9**(8), Art. no. 8, DOI: 10.1021/acscatal.9b01565.
4 X. Wang, *et al.*, Multiple Bioimaging Applications Based on the Excellent Properties of Nanodiamond: A Review, *Molecules*, 2023, **28**(10), 4063, DOI: 10.3390/molecules28104063.
5 S. A. Qureshi, W. W.-W. Hsiao, L. Hussain, H. Aman, T.-N. Le and M. Rafique, Recent Development of Fluorescent Nanodiamonds for Optical Biosensing and Disease Diagnosis, *Biosensors*, 2022, **12**(12), 1181, DOI: 10.3390/bios12121181.
6 M. Arruebo, R. Fernández-Pacheco, M. R. Ibarra and J. Santamaría, Magnetic nanoparticles for drug delivery, *Nano Today*, 2007, **2**(3), 22–32, DOI: 10.1016/S1748-0132(07)70084-1.
7 A. Salati, A. Ramazani and M. Almasi Kashi, Deciphering magnetic hyperthermia properties of compositionally and morphologically modulated FeNi nanoparticles using first-order reversal curve analysis, *Nanotechnology*, 2019, **30**(2), 025707, DOI: 10.1088/1361-6528/aae7f3.
8 H. B. Na, I. C. Song and T. Hyeon, Inorganic Nanoparticles for MRI Contrast Agents, *Adv. Mater.*, 2009, **21**(21), 2133–2148, DOI: 10.1002/adma.200802366.
9 V. N. Mochalin, O. Shenderova, D. Ho and Y. Gogotsi, The properties and applications of nanodiamonds, *Nat. Nanotechnol.*, 2012, **7**(1), Art. no. 1, DOI: 10.1038/nnano.2011.209.
10 A. B. Bourlinos, *et al.*, Fabrication of fluorescent nanodiamond@C core–shell hybrids *via* mild carbonization of sodium cholate–nanodiamond complexes, *J. Mater. Sci.*, 2011, **46**(24), Art. no. 24, DOI: 10.1007/s10853-011-5911-z.
11 M. Zeiger, N. Jäckel, V. N. Mochalin and V. Presser, Review: carbon onions for electrochemical energy storage, *J. Mater. Chem. A*, 2016, **4**(9), 3172–3196, DOI: 10.1039/C5TA08295A.
12 J. Tuček, K. C. Kemp, K. S. Kim and R. Zbořil, Iron-Oxide-Supported Nanocarbon in Lithium-Ion Batteries, Medical, Catalytic, and Environmental Applications, *ACS Nano*, 2014, **8**(8), 7571–7612, DOI: 10.1021/nn501836x.
13 M. Alahmadi and M. Siaj, Graphene-Assisted Magnetic Iron Carbide Nanoparticle Growth, *ACS Appl. Nano Mater.*, 2018, **1**(12), 7000–7005, DOI: 10.1021/acsanm.8b01794.
14 C. E. Guillaume, The Anomaly of the Nickel-Steels, *Proc. Phys. Soc., London*, 1919, **32**(1), 374–404, DOI: 10.1088/1478-7814/32/1/337.
15 A. Sahoo and V. R. R. Medicherla, Fe–Ni Invar alloys: A review, *Mater. Today: Proc.*, 2021, **43**, 2242–2244, DOI: 10.1016/j.matpr.2020.12.527.
16 J. I. Goldstein, The formation of the kamacite phase in metallic meteorites, *J. Geophys. Res.*, 1965, **70**(24), 6223–6232, DOI: 10.1029/JZ070i024p06223.
17 F. D. Stacey, S. K. Banerjee and F. D. Stacey, The physical principles of rock magnetism, *Developments in solid earth geophysics, no. v. 5*, Elsevier Scientific Pub. Co, Amsterdam New York, 1974.
18 D. G. Rancourt and R. B. Scorzelli, Low-spin γ-Fe-Ni(γLS) proposed as a new mineral in Fe-Ni-bearing meteorites: epitaxial intergrowth of γLS and tetrataenite as a possible equilibrium state at ∼20–40 at% Ni, *J. Magn. Magn. Mater.*, 1995, **150**(1), 30–36, DOI: 10.1016/0304-8853(95)00089-5.
19 L. J. Swartzendruber, V. P. Itkin and C. B. Alcock, The Fe–Ni (iron–nickel) system, *J. Phase Equilib.*, 1991, **12**(3), 288–312, DOI: 10.1007/BF02649918.
20 Y. A. Abdu, T. Ericsson and H. Annersten, Coexisting antiferromagnetism and ferromagnetism in mechanically alloyed Fe-rich Fe–Ni alloys: implications regarding the Fe–Ni phase diagram below 400 °C, *J. Magn. Magn. Mater.*, 2004, **280**(2–3), 395–403, DOI: 10.1016/j.jmmm.2004.03.036.
21 J. F. Albertsen, J. M. Knudsen, N. O. Roy-Poulsen and L. Vistisen, Meteorites and Thermodynamic Equilibrium in f.c.c. Iron–Nickel Alloys (25–50% Ni), *Phys. Scr.*, 1980, **22**(2), 171–175, DOI: 10.1088/0031-8949/22/2/014.
22 J. F. Albertsen, H. P. Nielsen and V. F. Buchwald, On the Fine Structure of Meteoritical Taenite/Tetrataenite and its Interpretation, *Phys. Scr.*, 1983, **27**(4), 314–320, DOI: 10.1088/0031-8949/27/4/015.
23 J. F. Albertsen, J. M. Knudsen and G. B. Jensen, Structure of taenite in two iron meteorites, *Nature*, 1978, **273**(5662), 453–454, DOI: 10.1038/273453a0.
24 R. B. Scorzelli and J. Danon, Mössbauer Spectroscopy and X-Ray Diffraction Studies of Fe–Ni Order-Disorder Processes in a 35% Ni Meteorite (Santa Catharina), *Phys. Scr.*, 1985, **32**(2), 143–148, DOI: 10.1088/0031-8949/32/2/010.
25 R. B. Scorzelli, *Hyperfine Interact.*, 1997, **110**(1/2), 143–150, DOI: 10.1023/A:1012679517295.
26 R. B. Scorzelli and E. Dos Santos, Meteoritic Fe–Ni alloys: A review of 57Fe Mössbauer spectroscopy studies, *Geochemistry*, 2019, **79**(4), 125547, DOI: 10.1016/j.chemer.2019.125547.
27 J. Paulevé, D. Dautreppe, J. Laugier and L. Néel, Une nouvelle transition ordre-désordre dans Fe–Ni (50-50),

J. Phys. Radium, 1962, **23**(10), 841–843, DOI: **10.1051/jphysrad:019620023010084100**.

28 L.-Y. Tian, *et al.*, Density Functional Theory description of the order-disorder transformation in Fe–Ni, *Sci. Rep.*, 2019, **9**(1), 8172, DOI: **10.1038/s41598-019-44506-7**.

29 G. J. Dienes and A. C. Damask, Radiation Enhanced Diffusion in Solids, *J. Appl. Phys.*, 1958, **29**(12), 1713–1721, DOI: **10.1063/1.1723032**.

30 A. Christiansen, L. Larsen, H. Roy-Poulsen, N. O. Roy-Poulsen, L. Vistisen and J. M. Knudsen, Iron–Nickel Alloys in a Taenite Lamella from the Iron Meteorite Cape York as Measured by Conversion Electron Mössbauer Spectroscopy, *Phys. Scr.*, 1984, **29**(1), 94–96, DOI: **10.1088/0031-8949/29/1/016**.

31 A. Kovács, *et al.*, Discovery and Implications of Hidden Atomic-Scale Structure in a Metallic Meteorite, *Nano Lett.*, 2021, **21**(19), 8135–8142, DOI: **10.1021/acs.nanolett.1c02573**.

32 M. Gong and S. Ren, Phase Transformation-Driven Surface Reconstruction of FeNi Nanostructures, *Chem. Mater.*, 2015, **27**(22), 7795–7800, DOI: **10.1021/acs.chemmater.5b03736**.

33 S. Goto, *et al.*, Synthesis of single-phase L10-FeNi magnet powder by nitrogen insertion and topotactic extraction, *Sci. Rep.*, 2017, **7**(1), 13216, DOI: **10.1038/s41598-017-13562-2**.

34 Y. Miura, S. Ozaki, Y. Kuwahara, M. Tsujikawa, K. Abe and M. Shirai, The origin of perpendicular magneto-crystalline anisotropy in $L1_0$–FeNi under tetragonal distortion, *J. Phys.: Condens. Matter*, 2013, **25**(10), 106005, DOI: **10.1088/0953-8984/25/10/106005**.

35 M. Werwiński and W. Marciniak, *Ab initio* study of magnetocrystalline anisotropy, magnetostriction, and Fermi surface of $L1_0$ FeNi (tetrataenite), *J. Phys. D: Appl. Phys.*, 2017, **50**(49), 495008, DOI: **10.1088/1361-6463/aa958a**.

36 A. M. Montes-Arango, *et al.*, Discovery of process-induced tetragonality in equiatomic ferromagnetic FeNi, *Acta Mater.*, 2016, **116**, 263–269, DOI: **10.1016/j.actamat.2016.06.050**.

37 X. G. Liu, D. Y. Geng, C. J. Choi, J. C. Kim and Z. D. Zhang, Magnetic properties, complex permittivity and permeability of FeNi nanoparticles and FeNi/AlO_x nanocapsules, *J. Nanopart. Res.*, 2009, **11**(8), 2097–2104, DOI: **10.1007/s11051-008-9575-9**.

38 E. Kaniukov, *et al.*, FeNi nanotubes: perspective tool for targeted delivery, *Appl. Nanosci.*, 2019, **9**(5), 835–844, DOI: **10.1007/s13204-018-0762-4**.

39 T. Hasegawa, T. Niibori, Y. Takemasa and M. Oikawa, Stabilisation of tetragonal FeCo structure with high magnetic anisotropy by the addition of V and N elements, *Sci. Rep.*, 2019, **9**(1), Art. no. 1, DOI: **10.1038/s41598-019-41825-7**.

40 T. Hasegawa and Y. Seki, TEM-based crystal structure analysis of body-centered tetragonal structure in non-epitaxial FeCo film with added V and N, *Mater. Lett.*, 2022, **313**, 131734, DOI: **10.1016/j.matlet.2022.131734**.

41 I. Z. Hlova, O. Dolotko, M. Abramchuk, A. Biswas, Y. Mudryk and V. K. Pecharsky, Enhancement of hard magnetism and chemical order of synthetic L10-FeNi, *J. Alloys Compd.*, 2024, 173619, DOI: **10.1016/j.jallcom.2024.173619**.

42 F. Takata, K. Ito and T. Suemasu, Fabrication of ordered Fe–Ni nitride film with equiatomic Fe/Ni ratio, *Jpn. J. Appl. Phys.*, 2018, **57**(5), 058004, DOI: **10.7567/JJAP.57.058004**.

43 D. Guenzburger and J. Terra, Theoretical study of magnetism and Mössbauer hyperfine interactions in ordered FeNi and disordered fcc Fe-rich Fe–Ni alloys, *Phys. Rev. B:Condens. Matter Mater. Phys.*, 2005, **72**(2), 024408, DOI: **10.1103/PhysRevB.72.024408**.

44 H. Piet *et al.*, *Superstoichiometric Alloying of H and Close-Packed FeNi under High Pressures: Implications for Hydrogen Storage in Planetary Cores*, In Review, preprint, 2020, DOI: **10.21203/rs.3.rs-103113/v1**.

45 P. Rani, J. Thakur, A. Taya and M. K. Kashyap, *Effect of tetragonal distortion induced by interstitial C-doping in L10-FeNi*, presented at the DAE SOLID STATE PHYSICS SYMPOSIUM 2018, Hisar, Haryana, India, 2019, p. 030497, DOI: **10.1063/1.5113336**.

46 A. P. Douvalis, A. B. Bourlinos, J. Tucek, K. Čépe, T. Bakas and R. Zboril, Development of novel FePt/nanodiamond hybrid nanostructures: L10 phase size-growth suppression and magnetic properties, *J. Nanopart. Res.*, 2016, **18**(5), Art. no. 5, DOI: **10.1007/s11051-016-3424-z**.

47 P. Ziogas, A. B. Bourlinos, J. Tucek, O. Malina and A. P. Douvalis, Novel Magnetic Nanohybrids: From Iron Oxide to Iron Carbide Nanoparticles Grown on Nanodiamonds, *Magnetochemistry*, 2020, **6**(4), Art. no. 4, DOI: **10.3390/magnetochemistry6040073**.

48 P. Ziogas, *et al.*, Intriguing Prospects of a Novel Magnetic Nanohybrid Material: Ferromagnetic FeRh Nanoparticles Grown on Nanodiamonds, *Metals*, 2022, **12**(8), 1355, DOI: **10.3390/met12081355**.

49 P. G. Ziogas, A. B. Bourlinos, P. Chatzopoulou, G. P. Dimitrakopulos, A. Markou and A. P. Douvalis, Novel Hybrid Ferromagnetic Fe–Co/Nanodiamond Nanostructures: Influence of Carbon on Their Structural and Magnetic Properties, *Magnetochemistry*, 2024, **10**(5), 35, DOI: **10.3390/magnetochemistry10050035**.

50 R. M. Cornell and U. Schwertmann, *The Iron Oxides: Structure, Properties, Reactions, Occurences and Uses*, Wiley, 1st edn, 2003, DOI: **10.1002/3527602097**.

51 B. D. Cullity and S. R. Stock, *Elements of X-ray diffraction*, Prentice Hall, Upper Saddle River, NJ, 3rd edn, 2001.

52 I. S. Lyubutin, C. R. Lin, Yu. V. Korzhetskiy, T. V. Dmitrieva and R. K. Chiang, Mössbauer spectroscopy and magnetic properties of hematite/magnetite nanocomposites, *J. Appl. Phys.*, 2009, **106**(3), Art. no. 3, DOI: **10.1063/1.3194316**.

53 L. K. Bogart, I. G. Morozov, I. P. Parkin and M. V. Kuznetcov, 57Fe Mössbauer study of NiFe2O4 nanoparticles produced by the levitation-jet aerosol technique, *J. Mater. Sci.: Mater. Electron.*, 2018, **29**(16), 14347–14352, DOI: **10.1007/s10854-018-9569-z**.

54 T. Komatsu and N. Soga, Mössbauer study of the NiFe2O4 precipitation process from a silicate glass, *J. Appl. Phys.*, 1980, **51**(1), 601–606, DOI: **10.1063/1.327312**.

55 J. H. Liu, L. Wang and F. S. Li, Magnetic properties and Mössbauer studies of nanosized NiFe2O4 particles, *J. Mater.*

Sci., 2005, **40**(9–10), 2573–2575, DOI: 10.1007/s10853-005-2077-6.

56 M. V. Ushakov, B. Senthilkumar, R. Kalai Selvan, I. Felner and M. I. Oshtrakh, Mössbauer spectroscopy of NiFe2O4 nanoparticles: The effect of Ni^{2+} in the Fe^{3+} local microenvironment in both tetrahedral and octahedral sites, *Mater. Chem. Phys.*, 2017, **202**, 159–168, DOI: 10.1016/j.matchemphys.2017.09.011.

57 N. N. Greenwood and T. C. Gibb, *Mössbauer Spectroscopy*, Springer, Netherlands, Dordrecht, 1971, DOI: 10.1007/978-94-009-5697-1.

58 P. Gütlich, E. Bill and A. X. Trautwein, *Mössbauer Spectroscopy and Transition Metal Chemistry*, Springer Berlin Heidelberg, Berlin, Heidelberg, 2011, DOI: 10.1007/978-3-540-88428-6.

59 S. Mørup and M. Hansen, *Superparamagnetic Particles*, 2007, DOI: 10.1002/9780470022184.hmm409.

60 S. Mørup, M. F. Hansen and C. Frandsen, Magnetic interactions between nanoparticles, *Beilstein J. Nanotechnol.*, 2010, **1**, 182–190, DOI: 10.3762/bjnano.1.22.

61 J. W. Drijver, K. De Groot and F. Van Der Woude, Determination Of Long Range Order In Ni_3 Fe Using The Mössbauer Effect Technique, *J. Phys. Colloq.*, 1974, **35**(C6), C6-465–C6-468, DOI: 10.1051/jphyscol:1974696.

62 M. Kanashiro and N. Kunitomi, Environment effect on the hyperfine field distributions in ordered Ni_3Fe, *Solid State Commun.*, 1976, **19**(11), 1127–1130, DOI: 10.1016/0038-1098(76)90114-9.

63 M. Kanashiro and N. Kunitomi, Non-Linear Local Environment Effect in Ni_3 Fe Observed by Mössbauer Effect of Fe^{57}, *J. Phys. Soc. Jpn.*, 1980, **48**(1), 93–101, DOI: 10.1143/JPSJ.48.93.

64 T. E. Cranshaw, The electronic and magnetic structure of ordered Ni_3 Fe studied by Mössbauer spectroscopy, *J. Phys. F: Met. Phys.*, 1987, **17**(4), 967–984, DOI: 10.1088/0305-4608/17/4/022.

65 B. Zhang, N.-E. Fenineche, H. Liao and C. Coddet, Magnetic properties of *in situ* synthesized $FeNi_3$ by selective laser melting Fe-80%Ni powders, *J. Magn. Magn. Mater.*, 2013, **336**, 49–54, DOI: 10.1016/j.jmmm.2013.02.014.

66 C.-W. Yang, D. B. Williams and J. I. Goldstein, A revision of the Fe–Ni phase diagram at low temperatures (<400 °C), *J. Phase Equilib.*, 1996, **17**(6), 522–531, DOI: 10.1007/BF02665999.

67 E. Dos Santos, J. Gattacceca, P. Rochette and R. B. Scorzelli G. Fillion, Magnetic hysteresis properties and 57Fe Mössbauer spectroscopy of iron and stony-iron meteorites: Implications for mineralogy and thermal history, Phys. Earth Planet. Inter., 2015, **242**, 50–64, DOI: 10.1016/j.pepi.2015.01.004.

68 G. V. Kurdjumov and A. G. Khachaturyan, Nature of axial ratio anomalies of the martensite lattice and mechanism of diffusionless $\gamma \rightarrow \alpha$ transformation, *Acta Metall.*, 1975, **23**(9), 1077–1088, DOI: 10.1016/0001-6160(75)90112-1.

69 V. G. Gavriljuk, *et al.*, Carbon Distribution in Low-Temperature Isothermal Iron-Based Martensite and Its Tetragonality, *Metallofiz. Noveishie Tekhnol.*, 2016, **38**(4), 455–475, DOI: 10.15407/mfint.38.04.0455.

70 V. G. Gavriljuk, A. V. Tarasenko and A. I. Tyshchenko, Low temperature ageing of the freshly formed Fe-C and Fe-N martensites, *Scr. Mater.*, 2000, **43**(3), 233–238, DOI: 10.1016/S1359-6462(00)00396-1.

71 R. N. Panda and N. S. Gajbhiye, Magnetic properties of nanocrystalline γ-Fe–Ni–N nitride systems, *J. Appl. Phys.*, 1999, **86**(6), 3295–3302, DOI: 10.1063/1.371205.

72 T. Sohmura and F. E. Fujita, Mössbauer effect in hydrogenated Fe–Ni alloys, *J. Phys. F: Met. Phys.*, 1978, **8**(9), 2061–2071, DOI: 10.1088/0305-4608/8/9/027.

73 J. Foct, P. Rochegude and C. Cordier-Robert, Atom distributions in mixed interstitial-substitutional solid solution: The case of Fe1−xNixNy austenite, *Hyperfine Interact.*, 1989, **45**(1–4), 359–364, DOI: 10.1007/BF02405900.

74 V. M. Nadutov, Mössbauer analysis of the effect of substitutional atoms on the electronic charge distribution in nitrogen and carbon austenites, *Mater. Sci. Eng., A*, 1998, **254**(1–2), 234–241, DOI: 10.1016/S0921-5093(98)00663-7.

75 L. Vergara, J. Desimoni, K. Laneri, A. Fernández Guillermet and G. J. Zarragoicoechea, Distribution of interstitial atoms in FCC Fe–N alloys: A Mössbauer, thermodynamic and Monte Carlo approach, *Phys. B*, 2005, **363**(1–4), 178–189, DOI: 10.1016/j.physb.2005.03.019.

76 P. M. Gielen and R. Kaplow, Mössbauer effect in iron-carbon and iron-nitrogen alloys, *Acta Metall.*, 1967, **15**(1), 49–63, DOI: 10.1016/0001-6160(67)90155-1.

77 W. K. Choo and R. Kaplow, Mössbauer measurements on the aging of iron-carbon martensite, *Acta Metall.*, 1973, **21**(6), 725–732, DOI: 10.1016/0001-6160(73)90036-9.

78 A. P. Douvalis, A. Polymeros and T. Bakas, IMSG09: A ^{57}Fe-^{119}Sn Mössbauer spectra computer fitting program with novel interactive user interface, *J. Phys.: Conf. Ser.*, 2010, **217**, 012014, DOI: 10.1088/1742-6596/217/1/012014.

79 G. Hongxia, C. Hua, L. Fan, Q. Zhenping, C. Suping and N. Zuoren, Shape-controlled synthesis of $FeNi_3$ nanoparticles by ambient chemical reduction and their magnetic properties, *J. Mater. Res.*, 2012, **27**(11), 1522–1530, DOI: 10.1557/jmr.2012.67.

80 X.-M. Zhou and X.-W. Wei, Single Crystalline $FeNi_3$ Dendrites: Large Scale Synthesis, Formation Mechanism, and Magnetic Properties, *Cryst. Growth Des.*, 2009, **9**(1), 7–12, DOI: 10.1021/cg8000976.

81 M. Nirouei, A. Jafari and K. Boustani, Magnetic and Structural Study of $FeNi_3$ Nanoparticles: Effect of Calcination Temperature, *J. Supercond. Novel Magn.*, 2014, **27**(12), 2803–2811, DOI: 10.1007/s10948-014-2727-5.

82 Surface effects in magnetic nanoparticles, in *Nanostructure science and technology*, ed. D. Fiorani, Springer, New York, 2005.

83 B. D. Cullity and C. D. Graham, *Introduction to Magnetic Materials*, Wiley, 1st edn, 2008, DOI: 10.1002/9780470386323.

84 O. A. Shenderova and G. E. McGuire, Science and engineering of nanodiamond particle surfaces for biological applications (Review), *Biointerphases*, 2015, **10**(3), 030802, DOI: 10.1116/1.4927679.

85 A. S. Barnard, Stability of Diamond at the Nanoscale, *Ultananocrystalline Diamond*, Elsevier, 2012, pp. 3–52, DOI: 10.1016/B978-1-4377-3465-2.00001-3.

86 T. Petit, J.-C. Arnault, H. A. Girard, M. Sennour and P. Bergonzo, Early stages of surface graphitization on nanodiamond probed by x-ray photoelectron spectroscopy, *Phys. Rev. B:Condens. Matter Mater. Phys.*, 2011, **84**(23), 233407, DOI: 10.1103/PhysRevB.84.233407.

87 P. W. Atkins, J. De Paula and J. Keeler, *Atkins' physical chemistry*, Oxford University Press, New York, NY, 12th edn, 2023.

88 A. Wiltner and C. Linsmeier, Formation of endothermic carbides on iron and nickel, *Phys. Status Solidi A*, 2004, **201**(5), 881–887, DOI: 10.1002/pssa.200304362.

89 A. M. Sherman, G. T. Eldis and M. Cohen, The Aging and Tempering of Iron–Nickel–Carbon Martensites, *Metall. Trans. A*, 1983, **14**(5), 995–1005, DOI: 10.1007/BF02659847.

90 J. Gautam, T. D. Thanh, K. Maiti, N. H. Kim and J. H. Lee, Highly efficient electrocatalyst of N-doped graphene-encapsulated cobalt-iron carbides towards oxygen reduction reaction, *Carbon*, 2018, **137**, 358–367, DOI: 10.1016/j.carbon.2018.05.042.

91 K. Y. Kim, *et al.*, Cobalt Ferrite Nanoparticles to Form a Catalytic Co–Fe Alloy Carbide Phase for Selective CO_2 Hydrogenation to Light Olefins, *ACS Catal.*, 2020, **10**(15), 8660–8671, DOI: 10.1021/acscatal.0c01417.

92 E. R. D. Scott, New Carbide, $(Fe,Ni)_{23}C_6$, found in Iron Meteorites, *Nat. Phys. Sci.*, 1971, **229**(2), 61–62, DOI: 10.1038/physci229061a0.

93 *Diffusion Bonding of Materials*, ed. N. F. Kazakov, Elsevier, 1985, DOI: 10.1016/C2013-0-03774-7.

94 R. Filipek, M. Danielewski and R. Bachorczyk Nagy, Interdiffusion Studies in Co–Fe–Ni Alloys, *Defect Diffus. Forum*, 2005, **237–240**, 408–413, DOI: 10.4028/www.scientific.net/DDF.237-240.408.

95 K. L. Crispin, S. Saha, D. Morgan and J. A. Van Orman, Diffusion of transition metals in periclase by experiment and first-principles, with implications for core–mantle equilibration during metal percolation, *Earth Planet. Sci. Lett.*, 2012, **357–358**, 42–53, DOI: 10.1016/j.epsl.2012.09.023.

96 A. Bourlinos, A. Simopoulos, D. Petridis, H. Okumura and G. Hadjipanayis, Silica-Maghemite Nanocomposites, *Adv. Mater.*, 2001, **13**(4), 289–291, DOI: 10.1002/1521-4095(200102)13:4<289::AID-ADMA289>3.0.CO;2-U.